Predissociation dynamics and infrared absorption spectra of Li^+-H_2 and Li^+-D_2 complexes

A close-coupling study

Felicja Mrugała

Institute of Physics, Faculty of Physics, Astronomy and Informatics,
Nicolaus Copernicus University,

Toruń, 2021

I. INTRODUCTION

Facts motivating the study:

(i) availability of experimental data on rotationally resolved infrared spectra of the complexes in the H-H (D-D) excitation regions [C. D . Thompson, C. Emmeluth, B. L. J. Poad, G. H. Weddle, and E. J. Bieske, J. Chem. Phys. **125**, 044310 (2006); C. Emmeluth, B. L. J. Poad, C. D. Thompson, G. H. Weddle, and E. J. Bieske, J. Chem. Phys. **126** 204309 (2007)].

(ii) only two theoretical simulations (one for each complex) existing which can be confronted with the measured transitions energies [A. J. Page and E. I. von Nagy-Felsobuki, J. Phys. Chem. **A 111**, 4478 (2007); Theor. Chem. Acc. **122**, 87 (2009)]. The consistency is much less satisfactory than that achieved for other complexes of atomic metal cations (M^+) with H_2 and D_2 in the studies reviewed in: V. Dryza and E. J. Bieske, Intern. Rev. Phys. Chem. **32**, 559 (2013).

(iii) availability of electronic structure data for the potential energy and electric dipole moment surfaces of the ground electronic state of the $[LiHH]^+$ system which, despite encouraging accuracy of results of the introductory application [W. P. Kraemer and V. Špirko, Chem. Phys. **330**, 190 (2006)], have not been exploited in any other more extensive calculations on dynamics and spectroscopy of the complexes.

(iv) similarity of the title complexes to the He^+-H_2 complex whose dynamics was quite extensively investigated in the course of the studies on radiative association and charge transfer reactions in the $He^+ + H_2$ gas mixtures at low temperatures (<100 K) [F. Mrugała and W. P. Kraemer, J. Chem. Phys. **122**, 224321 (2005); **138**, 104315 (2013)]. The tools elaborated for those studies should to be also useful in calculations on complexes of the M^+-H_2 type.

The goals:

(i) improve consistency of theoretical simulations with the 2006-7 measurements of Bieske *et al.* on the title complexes,

(ii) provide some predictions for the planned/expected (Ref. 1,2) experimental investigations of other aspects of spectroscopy and dynamics of the M^+-H_2 type complexes, such as absorption from/to states excited in the intermolecular stretching and/or bending modes, vibrational predissociation rates, populations of product rotational states.

(iii) propose some methodological improvements for calculations on dynamics (predissociating states) of atom-diatom complexes.

The approaches:

- **'exact':** solving the time-independent Schroedinger equation within the close-coupling (CC) approximation. Two formulations of the CC equations are exploited:
  - 'BF-diabatic' — the standard formulation using body-fixed reference frame and diabatic basis for description of bounded motions,
  - 'SF-adiabatic' — formulation using a ro-vibrationally adiabatic basis, closely related to the popular adiabatic bender approximation [S. L. Holmgren, M. Waldman, and W. Klemperer, J. Chem. Phys.67, 4414(1977)]. The associated non-adiabatic couplings are not neglected, however. They are effectively accounted for by making use of the smooth-variable discretization (SVD) technique [O. I. Tolstikhin, S. Watanabe, and M. Matsuzawa, J. Phys. **B29**, L389 (1996)].
- **approximate:** evaluating formulas of the perturbative resonance theory of Fano. The purpose: to assist analysis of the CC results on vibrational predissociation of the complexes.

The computational methods: algorithms of the generalized log-derivative method [F. Mrugała, Int. Rev. Phys. Chem. **12**, 1 (1993)], especially the versions for equations in quasi-diabatic representations which are easily adaptable to the SVD technique.

II. OUTLINE of THEORY

The configuration of the nuclear centers in the Li^++a_2 (a=H,D) system is described by three coordinates r, R, and θ being the lengths and the angle between the Jacobi vectors $\mathbf{r}$ and $\mathbf{R}$ which join, respectively, the nuclei in a_2 (protons, deuterons) and the center-of-mass of the a_2 with the Li nucleus. The orientation of the plane of the three nuclei is described by azimuthal (α) and spherical (β) angles of the vector $\mathbf{R}$ with respect to a space-fixed (SF) reference frame $Oxyz$ with the origin O at the center-of-mass of a-a-Li and by angle (ψ) of rotation of the plane around $\mathbf{R}$. Euler rotations of the SF frame over the angles α, β, and ψ give a body-fixed (BF) reference frame $OXYZ$ with the axis Z aligned to $\mathbf{R}$ and the axis Y perpendicular to the plane of the nuclei. The azimuthal and spherical angles of the vector $\boldsymbol{r}$ in the two frames are $(\alpha_r,\beta_r):=\widehat{\mathbf{r}}_{\rm SF}$ and $(0,\theta)$, respectively. (ψ,θ), denoted with $\widehat{\mathbf{r}}_{\rm BF}$, are the angles in the partly body-fixed frame which is related to $Oxyz$ by the Euler angles $(\alpha,\beta,0):=(\widehat{\mathbf{R}},0)$.

The Hamiltonian for the relative nuclear motion in the Li^++a_2 system is $H=K+\overline{V}=H_0+V$, where K denotes the kinetic energy operator, $\overline{V}(r,R,\theta)$ — the electronic energy potential surface (PES), H_0 is the Hamiltonian of the noninteracting subunits, and $V(r,R,\theta)$ — the interaction potential obtained by subtracting from $\overline{V}$ the part $\underset{R\to\infty}{\overline{V}}:=V_{\rm HH}(r)$. Expressed in the Jacobi vectors, $K(\mathbf{R},\mathbf{r})=-\frac{\hbar^2}{2\mu}\Delta(\mathbf{R})-\frac{\hbar^2}{2m}\Delta(\mathbf{r})$, where μ and m are the reduced masses of Li^+–a_2 and of a-a, respectively, and $H_0(\mathbf{R},\mathbf{r})=-\frac{\hbar^2}{2\mu}\Delta(\mathbf{R})+H_{\rm HH}(\mathbf{r})$. The vibrational and translational modes of motion in the system are described by the radial coordinates r and R, and the rotational motions are described by the four angles $\widehat{\mathbf{R}}$ and $\widehat{\mathbf{r}}_{\rm SF}$ or $\widehat{\mathbf{R}}$ and $\widehat{\mathbf{r}}_{\rm BF}$. Expressed in the $(R,r,\widehat{\mathbf{R}},\widehat{\mathbf{r}}_{\rm fr})$ coordinates, for fr=BF or SF, the kinetic energy operator is[11,12],

$$K(R,r,\widehat{\mathbf{R}},\widehat{\mathbf{r}}_{\rm fr}) = \frac{1}{2\mu}\left[p^2(R)+\frac{1}{R^2}\,{}_{\rm fr}\mathbf{L}^2(\widehat{\mathbf{R}},\widehat{\mathbf{r}}_{\rm fr})\right]+\frac{1}{2m}\left[p^2(r)+\frac{1}{r^2}\,\mathbf{j}^2(\widehat{\mathbf{r}}_{\rm fr})\right], \qquad (1)$$

where $p(x)=-\imath\hbar(\frac{\partial}{\partial x}+\frac{1}{x})$ for $x=R,r$ are the radial momenta operators and the operators in the angular coordinates have the following meaning. ${}_{\rm SF}\mathbf{L}=\mathbf{J}(\widehat{\mathbf{R}},0)$ and $\mathbf{j}(\widehat{\mathbf{r}}_{\rm SF})=\mathbf{J}(\widehat{\mathbf{r}}_{\rm SF},0)$ are the angular momenta $\mathbf{l}$ and $\mathbf{j}$ of the Li^+ ion about the a_2 diatom and of the a_2 rotations, respectively, and ${}_{\rm BF}\mathbf{L}^2=\mathbf{J}^2(\widehat{\mathbf{R}},\psi)+\mathbf{j}^2(\widehat{\mathbf{r}}_{\rm BF})-2\sum_{\epsilon=-1}^{1}\mathcal{P}_{-\epsilon}(\widehat{\mathbf{R}},\psi)e^{-\imath\epsilon\psi}j_\epsilon(\widehat{\mathbf{r}}_{\rm BF})$. The symbol $\mathbf{J}(\widehat{\mathbf{R}},\psi)$ denotes the set of the differential operators $(\mathcal{J}_x,\mathcal{J}_y,\mathcal{J}_z)$ which represent the total angular momentum $\mathbf{J}=\mathbf{l}+\mathbf{j}$ in the SF basis vectors and the symbols $\mathcal{P}_\epsilon$ for $\epsilon=\pm1,0$ are related to the operators $(\mathcal{P}_X,\mathcal{P}_Y,\mathcal{P}_Z)$ representing $\mathbf{J}$ in the BF basis vectors[13]. $\mathbf{J}^2=\sum_{\epsilon=-1}^{1}\mathcal{J}_\epsilon\mathcal{J}_{-\epsilon}=\sum_{\epsilon=-1}^{1}\mathcal{P}_\epsilon\mathcal{P}_{-\epsilon}$, where $\mathcal{J}_{\pm1}=\frac{1}{\sqrt{2}}(\mathcal{J}_x\pm\imath\mathcal{J}_y)$, $\mathcal{J}_0=\mathcal{J}_z$, and $\mathcal{P}_\epsilon(\alpha,\beta,\psi)=J_{-\epsilon}(\psi,-\beta,\alpha)$. The other symbols denote: $\mathbf{j}^2(\widehat{\mathbf{r}}_{\rm fr})=\mathbf{J}^2(\widehat{\mathbf{r}}_{\rm fr},0)$ and $j_\epsilon(\widehat{\mathbf{r}}_{\rm BF})=\mathcal{J}_\epsilon(\widehat{\mathbf{r}}_{\rm BF},0)$ for $\epsilon=\pm1,0$.

A. Ro-vibrational states of the Li^+-a_2 (a=H,D) complexes

The states of interest are bound and quasi-bound states of the Hamiltonian $H(\mathbf{r},\mathbf{R})$, $\Psi^{JMp}(E_n^{\rm B};\mathbf{r},\mathbf{R})$ and $\mathbf{\Psi}^{(+)JMp}(E_n^{\rm res};\mathbf{r},\mathbf{R})$, which are also eigenstates of the operators $\mathbf{J}^2$, J_z, $\mathcal{I}$ (spatial inversion), and P (permutation of identical nuclei) to the eigenvalues $\hbar^2J(J+1)$, $\hbar M$, $p\,(-1)^J$, and $(-1)^I$, respectively, where I denotes the nuclear spin of a_2 and $p=\pm1$ is the spectroscopic parity. More specifically, $\mathbf{\Psi}^{(+)JMp}(E_n^{\rm res};\mathbf{r},\mathbf{R})$ denotes the set of partial stationary scattering states $\left\{\langle\mathbf{r},\mathbf{R}|E^{(+)}JMp,(vjl)_i\rangle\,,\ i=1,\dots N_{\rm o}\right\}$ at energy of a resonance, $E=E_n^{\rm res}$. The symbols behind the comma in the ket indicate the related state (of H_0) before scattering[14] as being $|EJMp\,(vjl)_i\rangle$, where $E=E_{\rm kin}+\varepsilon_{(vj)_i}$ and the quantum numbers v, j, and l specify the occupied states of $H_{\rm HH}$, $\mathbf{j}^2$, and $\mathbf{l}^2$, respectively. $N_{\rm o}$ is the number of (vjl) states that at given E, J, p, and I pertain to open Li^++$a_2(I;v\,j)$-channels ($E_{\rm kin}>0$). Only channels with j of parity $(-1)^I$ are possible in the Li^++$a_2(I)$ system, where $I=0\,(1)$ and $I=1\,(0,2)$ for a_2 being para-(ortho-) H_2 and D_2, respectively.

The resonance energy $E_n^{\rm res}$ together with related resonance width Γ_n are precisely defined by referring to analytical properties of the partial scattering matrix, $\mathbf{S}^{Jp}(E)=\{\langle EJMp\,(vjl)_f|V|E^{(+)}JMp,(vjl)_i\rangle,\ \ i,f=1,\dots N_{\rm o}\}$, continued into complex energy plane[14]. Staying in the real energy domain, it is sufficient here to adopt definitions based on the isolated resonance decomposition[15] of $\mathbf{S}^{Jp}(E)$,

$$\boldsymbol{S}(E)=\mathbf{S}^{\rm d}(E)\left[\mathbf{I}-\imath\hbar^{-\frac{1}{2}}\boldsymbol{\gamma}^{\dagger}(E)\,\mathbf{a}(E)\right]\quad\text{with}\quad\mathbf{a}(E)=-\imath\frac{\sqrt{\hbar}\boldsymbol{\gamma}(E)}{E-E^{\rm r}(E)+\frac{\imath}{2}\,\Gamma(E)}\,,\qquad(2)$$

where $\mathbf{I}$ denotes unit matrix and $\boldsymbol{\gamma}$ is $N_{\rm o}$-dim. row vector which satisfies the relation $\boldsymbol{\gamma}^{\rm T}=\mathbf{S}^{\rm d}\boldsymbol{\gamma}^{\dagger}$ and gives $\Gamma=\boldsymbol{\gamma}\boldsymbol{\gamma}^{\dagger}$. Namely, E is considered to be a resonance energy $E_n^{\rm res}$ if: $E^{\rm r}(E_n^{\rm res})=E_n^{\rm res}$, the functions $\Gamma(E)$ and $E^{\rm r}(E)$ are nearly constant at least in the interval $[E_n^{\rm res}-\Gamma_n, E_n^{\rm res}+\Gamma_n]$ with $\Gamma_n:=\Gamma(E_n^{\rm res})$, and the variation of $\mathbf{S}^{\rm d}(E)$ within this interval is slow. Then $P_{n,i}:=\Gamma_{n,i}/\Gamma_n$ with $\Gamma_{n,i}:=|\gamma_i(E_n^{\rm res})|^2$ gives the probability of decay of the quasi-bound state of Li^+–a_2 into the state $(vjl)_i$ of free Li^++a_2 system. Obviously, $\sum\limits_{l_i}P_{n,i}:=P_{n,vj}$ gives the population of decay channel $v\,j$.

For the actual determination of the quasi-bound state characteristics, the collision-time-delay (life-time) matrix[16] is used, $\boldsymbol{Q}^{Jp}=\imath\hbar(\boldsymbol{S}_E)^{\dagger}\boldsymbol{S}^{Jp}$; the subscript '$E$' denotes hereafter derivative with respect to energy. The isolated resonance decomposition of $\boldsymbol{S}^{Jp}(E)$ implies the following (exact) decomposition of $\boldsymbol{Q}^{Jp}(E)$

$$\boldsymbol{Q}(E)=\boldsymbol{Q}^{\rm d}(E)+\boldsymbol{Q}^{\rm r}(E)+\boldsymbol{q}(E)\quad\text{with}\quad\boldsymbol{Q}^{\rm r}(E)=\mathbf{a}^{\dagger}(E)\mathbf{a}(E)\,,\qquad(3)$$

$\boldsymbol{Q}^{\rm d}=\imath\hbar(\boldsymbol{S}_E^{\rm d})^{\dagger}\boldsymbol{S}^{\rm d}$, and $\boldsymbol{q}$ comprising terms proportional to $E_E^{\rm r}$ and $\boldsymbol{\gamma}_E$. A detailed description of this decomposition and of the entire life-time (LT) matrix approach to the resonance determination is enclosed in Supplementary Material, Ref. 55

The quantum numbers J and p and the formal index n are used above to differentiate between the ro-vibrational energy levels of the Li^+–$\mathrm{a}_2(I)$ complexes. It appears that in the majority of their bound and quasi-bound states the complexes behave like atom-diatom van der Waals molecules of intermediate anisotropy strength[17]. This allows for complete and meaningful labeling of the corresponding energy levels. Namely, the index n may be replaced with four approximate quantum numbers, v_r, b, k, and v_R, where v_r and b describe internal stretching and hindered rotations of the a_2 subunit and correlate with the vibrational (v) and rotational (j) quantum numbers of free a_2, v_R describes intermolecular stretching motion, and k denotes the absolute value of the best preserved eigenvalue λ of the angular momentum operator $\mathcal{P}_Z=\jmath_Z$. Possible values of k are: $k=k_{\rm min},\dots b$ with $k_{\rm min}=0\,(1)$ for $p=1\,(-1)$ or $e\,(f)$ parity states. In some states of the present complexes, however, rotations of the diatomic subunits are rather severely restricted. In consequence, a considerable j-mixing occurs in these states and assigning them with the number b, as defined above, becomes problematic. Therefore a vibrational bending number v_θ is also introduced. It is based on the Natural Expansion Analysis (NEA) of functions of the states[18,26] and is equal to the number of zeros which occur in the most populated natural orbital in the θ coordinate inside the $[0,\pi]$ interval. The number b may be defined as the sum v_θ+k and as such it remains meaningful for any state of the Li^+–$\mathrm{H}_2\,(\mathrm{D}_2)$ complexes. Considering only states with unexcited intermolecular vibration modes, v_R=0 and v_θ=0, the complexes have been treated in Refs. 3 and 4 as near-rigid asymmetric tops and the rotational levels have been labeled with the standard symbol[19] J_{K_a,K_c}. Since the body-fixed axes Z and X nearly coincide with the principal axes of the top a and b, respectively, and obviously Y coincides with the axis c, the numbers K_a and K_c can be obtained from the quantum numbers k, J and p as: K_a=k and K_c=$J-k+\frac{1-(-1)^s}{2}$ where $(-1)^s=(-1)^k p$ (s=0, 1 is the parity index of the asymmetric top functions[19]).

B. Characteristics of absorption spectrum

The cross-section for absorption of light of frequency ν by the Li^+–a_2 (a=H, or D) molecules in a gas at temperature T, or the absorption coefficient by one molecule in unit volume of

the gas[20,21], is the sum

$$\sigma(\nu;T) = \sum_{\rm i,f} \sigma_{\rm i\to f}(\nu;T) = \sum_{\rm i,f} I_{\rm i\to f}(T)\,\Phi(\nu{-}\nu_{\rm if})\,, \tag{4}$$

where $\sigma_{\rm i\to f}(\nu;T)$ is the cross-section due to transitions from states of energy $E_{\rm i}$ to states of energy $E_{\rm f}$, and the symbols appearing in the second equality are the characteristics of the corresponding absorption line: the position of its center, $\nu_{\rm if}{=}\frac{1}{hc}(E_{\rm f}{-}E_{\rm i})$ with h being the Planck constant and c — the speed of light, the absolute intensity, $I_{\rm i\to f}(T){=}\int \sigma_{\rm i\to f}(\nu;T)\,d\nu$, and the line profile, $\Phi(\nu{-}\nu_{\rm if})$. The profile is here a Lorentzian whose half-width-at-half-maximum accounts for dissociative decay of the final state in the transition, i.e. $\Phi(\nu{-}\nu_{\rm fi}){=}\frac{1}{\pi}\frac{\gamma}{(\nu-\nu_{\rm if})^2+\gamma^2}{:=}L_\gamma(\nu{-}\nu_{\rm if})$ with $\gamma{=}\Gamma/(2hc)$. [In the actual line shape simulations, the profiles $L_\gamma(\nu{-}\nu_{\rm if})$ were convoluted with a Gaussian to account for some other causes of broadening]. The intensity $I_{\rm i\to f}(T)$ is given by the formula

$$I_{\rm i\to f}(T){=}\Big\{\frac{2\pi^2}{3hc\epsilon_0}\Big\}\,\nu_{\rm if}\,S_{\rm i\to f}\,P_{\rm i}(T)\,[1{-}\exp(-hc\nu_{\rm if}/k_BT)] \tag{5}$$

and is related to the electric-dipole vector of the Li^+–H_2 molecule, $\mathbf{d}(\mathbf{r},\mathbf{R})$, through the factor $S_{\rm i\to f}$ — the line strength which is defined by the expression

$$S_{\rm i\to f}\,L_\gamma(\nu{-}\nu_{\rm if}) \approx hc\sum_q \sum_{M_{\rm f},M_{\rm i}} \langle\ldots|\ldots\rangle^\dagger \langle \mathbf{\Psi}^{(+)\,J_{\rm f}M_{\rm f}p_{\rm f}}(E)|d_q\Psi^{J_{\rm i}M_{\rm i}p_{\rm i}}(E_{\rm i}^{\rm B})\rangle \tag{6}$$

with d_q denoting spherical components of $\mathbf{d}$ with respect to SF-axes, $\nu{=}\frac{1}{hc}(E{-}E_{\rm i}^B)$, $\nu_{\rm if}{=}\frac{1}{hc}(E_{\rm f}^{\rm res}{-}E_{\rm i}^B)$, and $|\nu{-}\nu_{\rm if}|{\sim}\gamma$. The factor $P_{\rm i}(T)$, when multiplied by $(2J_{\rm i}{+}1)$, gives the population of the energy level $E_{\rm i}$ at temperature T,

$$P_{\rm i}(T) = g_{\rm i}\exp(-E_{\rm i}/k_{\rm B}T)/Z(T)\,; \tag{7}$$

here $g_{\rm i}$ is the nuclear spin statistical factor which assumes values 1 (3) or 3 (6) for 'i' being a state of Li^+–a_2 with a_2=para-(ortho-)H_2 or a_2=para-(ortho-)D_2, respectively, k_B is the Boltzmann constant, and $Z(T)$ — the total internal partition sum (TIPS),

$$Z(T) = \sum_{\rm i} g_{\rm i}(2J_{\rm i}{+}1)\exp(-E_{\rm i}/k_BT)\,. \tag{8}$$

The factor in braces in formula (5) with ϵ_0 being the permittivity of free space is $4.1623756{\times}10^{-19}$ cm^2 Debye^{-2}.

The integrated vibrational band intensity $I_{[{\rm v}'']\to[{\rm v}']}$ is the sum

$$I_{[{\rm v}'']\to[{\rm v}']}(T) = \sum_{k,J,p}\sum_{k',J',p'} I_{\rm i\to f}(T) \tag{9}$$

as the letter 'i' ('f') stands for the complete label ([v] $k\,J\,p$) with [v]:=[$v_r\,v_\theta\,v_R$] of the initial (final) rovibrational energy-level.

C. Close-coupling

Diabatic representations. In the standard implementations of the close-coupling approximation[22,23] to solving the time-independent Schrödinger equation with the Hamiltonian $H(R,r,\widehat{\mathbf{R}},\widehat{\mathbf{r}}_{\rm fr})$ for fr=SF and fr=BF, the dependencies on the five coordinates $(r,\widehat{\mathbf{R}},\widehat{\mathbf{r}}_{\rm fr}){:=}y_{\rm fr}$ are described using orthonormal bases ${}_{\rm fr}\underset{1\times N}{\mathbf{\Phi}}^{JMp}{=}\big\{\Phi_{vjL_{\rm fr}}^{JMp}(y_{\rm fr})\big\}$ the individual members of which are built of eigenfunctions of the operators $H_{\rm HH}$, $\mathbf{j}^2$, and $\mathbf{l}^2$ or $\jmath_Z$; the symbol $L_{\rm fr}$ stands for the quantum number l or λ (when fr=BF). In these bases, the Hamiltonian matrices take the form

$${}_{\rm fr}\mathbf{H}^{Jp}(R) = -\tfrac{\hbar^2}{2\mu}\mathbf{I}\tfrac{d^2}{dR^2} + {}_{\rm fr}\mathbf{W}^{Jp}(R)\,, \tag{10}$$

where the matrix ${}_{\rm fr}\mathbf{W}^{Jp}(R)$ contains couplings between the $(vjL_{\rm fr})$ states included. Explicit expressions for these couplings are listed in numerous papers. Here it suffices to remind only the structure of the matrix ${}_{\rm BF}\mathbf{W}^{Jp}(R)$,

$$\left[{}_{\rm BF}\mathbf{W}^{Jp}(R)\right]_{vj\lambda,\,v'j'\lambda'} = \delta_{v,v'}\delta_{j,j'}\,\frac{\hbar^2}{2\mu R^2}\left[\mathbf{c}^{Jp}(j)\right]_{\lambda,\lambda'} + \delta_{\lambda,\lambda'}\left[\delta_{v,v'}\delta_{j,j'}\,\varepsilon_{vj} + V^{\lambda}_{vj,\,v'j'}(R)\right]. \qquad (11)$$

The non-zero elements $\left[\mathbf{c}^{Jp}(j)\right]_{\lambda,\lambda'}$, for $\lambda'{=}\lambda$ and $\lambda'{=}\lambda{\pm}1$, are the coefficients of the centrifugal potentials and of the Coriolis couplings, $J(J{+}1){+}j(j{+}1){-}2\lambda^2$ and $-[J(J{+}1){-}\lambda(\lambda{\pm}1)]^{1/2}$, respectively, and $V^{\lambda}_{vj,\,v'j'}(R)$ is the potential coupling $\sum_L \langle vj|V_L(r,R)|v'j'\rangle_r\, g^{\lambda}_L(j,j')$, with V_L being the L-th order anisotropy strength function which comes from the Legendre polynomial expansion $V(r,R,\theta){=}\sum_L V_L(r,R)P_L(\cos\theta)$ and $g^{\lambda}_L(j,j'){=}(-1)^L C(jLj',000)C(j'Lj,\lambda 0\lambda)$, where $C(\ldots,\ldots)$ denotes the Clebsch-Gordan coefficient.

The size N of the matrices ${}_{\rm fr}\mathbf{H}^{Jp}$ for given J, p and I (not explicitly shown) is determined by the included vj states, $v{=}0,1,...,v_{\rm max}$ and $j{=}j_{\rm min}, j_{\rm min}{+}2, ..., j_{\rm max}$ with $j_{\rm min}=0\,(1)$ for I even (odd). For each j, the values of l may change in step of 2 from $|J{-}j|{+}\frac{1-p}{2}$ to $J{+}j{-}\frac{1-p}{2}$ and the values of λ may change in step of 1 from $\frac{1-p}{2}$ to $\min(J,j)$.

Formally, the two diabatic representations are equivalent, i.e. ${}_{\rm SF}\mathbf{\Phi}^{JMp}{=}{}_{\rm BF}\mathbf{\Phi}^{JMp}\,\mathbf{U}^{Jp}$ where $\mathbf{U}^{Jp}$ is a unitary transformation (see e.g. Ref. 24 for details). For practical reasons, however, the BF-diabatic representation is better suited to the present complexes. The reasons are:

(i) The assignment of the ro-vibrational energy levels with the approximate quantum numbers is greatly facilitated. Namely, in the matrices of radial functions ${}_{\rm BF}\mathbf{F}^{Jp}_{N\times 1}(E^B_n;R)$ and ${}_{\rm BF}\mathbf{F}^{(+)\,Jp}_{N\times N_{\rm o}}(E^{\rm res}_n;R)$ which represent the states $\Psi^{JMp}(E^{\rm B}_n;\mathbf{r},\mathbf{R})$ and $\mathbf{\Psi}^{(+)\,JMp}(E^{\rm res}_n;\mathbf{r},\mathbf{R})$, respectively, there are rows of clearly dominating components whose index (v,j,λ) contains the same values of v and λ. This gives the two approximate numbers v_r and k, respectively. In the majority of the states, single rows of dominating components occur and on this ground the number b can be assigned, too.

(ii) A good approximation is indicated and easy to implement. Namely, the radial functions with large values of λ appear rather unimportant for converging the calculated energies E^B_n, $E^{\rm res}_n$, and widths Γ_n. This allows for a reduction of the size N of the basis ${}_{\rm BF}\mathbf{\Phi}^{JMp}$. It is realized by excluding all functions $\Phi^{JMp}_{vj\lambda}$ with $\lambda{>}\lambda_{\rm max}$ where $\lambda_{\rm max}$ is a fixed value which may be much smaller than $j_{\rm max}$ but not smaller than the number b of state being calculated. The resulting approximation, called 'Coriolis-coupling-reducing' (CCr), is a part of the CC-BF-diabatic approach which was exploited in our calculations on the $He^+{+}H_2$ and $He{+}H_2^+$ systems[25–27].

Adiabatic representation. The adiabatic basis of interest here is the one introduced in Ref. 27 for the purpose of enabling a perturbative treatment of rotational predissociation in the He^+–H_2 complex. It is defined by means of orthogonal matrices ${}_{\rm fr}\mathbf{\Upsilon}^{Jp}_{N\times N}(R){=}\left\{\Upsilon^{Jp}_{vjL_{\rm fr},\bar{v}\bar{j}\bar{l}}(R)\right\}$ which diagonalize the coupling matrices ${}_{\rm fr}\mathbf{W}^{Jp}(R)$ at different Rs. Namely,

$$\mathbf{\Phi}^{JMp}_{1\times M}(y_{\rm SF};R){=}{}_{\rm fr}\mathbf{\Phi}^{JMp}(y_{\rm fr})\left[{}_{\rm fr}\mathbf{\Upsilon}^{Jp}(R)\right]_{N\times M} \qquad (12)$$

with $M{\le}N$. In this basis, the Hamiltonian H takes the form,

$$\mathbf{H}^{Jp}(R) = -\tfrac{\hbar^2}{2\mu}\left[\mathbf{I}\tfrac{d^2}{dR^2} + 2\mathbf{A}^{Jp}(R)\tfrac{d}{dR} + \mathbf{B}^{Jp}(R)\right] + \mathbf{e}^{Jp}(R)\,, \qquad (13)$$

where $\mathbf{e}^{Jp}(R)$ denotes a diagonal matrix of ro-vibrational adiabatic energies,

$$\mathbf{e}^{Jp}(R){:=}\left[{}_{\rm fr}\mathbf{\Upsilon}^{Jp\,T}(R)\,{}_{\rm fr}\mathbf{W}^{Jp}(R)\,{}_{\rm fr}\mathbf{\Upsilon}^{Jp}(R)\right]_{M\times M}, \qquad (14)$$

and $\mathbf{A}^{Jp}(R)$ and $\mathbf{B}^{Jp}(R)$ are the respective non-adiabatic coupling matrices,

$$\mathbf{A}^{Jp}(R) = \left[{}_{\rm fr}\mathbf{\Upsilon}^{Jp\,T}(R)\,\frac{d}{dR}\,{}_{\rm fr}\mathbf{\Upsilon}^{Jp}(R)\right]_{M\times M} \qquad \text{and} \qquad \mathbf{B}^{Jp}(R) = \left[\ldots\frac{d^2}{dR^2}\ldots\right]_{M\times M}. \tag{15}$$

At sufficiently large Rs, the matrices ${}_{\rm fr}\mathbf{\Upsilon}^{Jp}(R)$ become constant and equal to $\mathbf{I}$ when fr=SF and $\mathbf{U}^{Jp}$ when fr=BF. In consequence, $\mathbf{H}^{Jp}(R)$ becomes diagonal and the adiabatic energies behave like $e^{Jp}_{\bar{v}\bar{j}\bar{l}}(R) \underset{R\to\infty}{\longrightarrow} \varepsilon_{\bar{v}\bar{j}}+\frac{\hbar^2}{2\mu}(\Lambda^2_{\bar{l}}-\frac{1}{4})/R^2$, where $\Lambda^2_{\bar{l}}-\frac{1}{4}$ denotes an eigenvalue of the kinetic energy coupling matrix $\underset{n\times n}{\mathbf{c}^{Jp}(\bar{j})}$. If dimension of this matrix is as large as allowed, i.e., n=min$(J,\bar{j})+\frac{1+p}{2}$, all $\Lambda_{\bar{l}}$s assume half-integer values, $\Lambda_{\bar{l}}=\bar{l}+\frac{1}{2}$, and $\bar{l}$ correlates strictly with the quantum number l. If n is reduced because of the restriction $\lambda\leq\lambda_{\rm max}$ imposed in the construction of ${}_{\rm BF}\mathbf{W}^{Jp}$, i.e. the CCr approximation is applied prior to the diagonalization (which is computationally advantageous), non-half-integer $\Lambda_{\bar{l}}$s arise and $\bar{l}$ only enumerates them.

In the basis (12), called 'SF-adiabatic'[27], the eigenstates of the Hamiltonian H are represented by matrices of radial functions $\mathbf{F}^{Jp}(E;R)$ which obviously have to satisfy the coupled equations,

$$[E\mathbf{I}-\mathbf{H}^{Jp}(R)]\,\mathbf{F}^{Jp}(E;R)=0\,, \tag{16}$$

and should vanish at R=0. The behavior at large Rs depends on whether E belongs to the point part of the spectrum of H, in which case $\mathbf{F}^{Jp}(E^B_n;R) \underset{R\to\infty}{\longrightarrow} 0$, or E lies in the continuum part. In the latter case, the conditions appropriate for partial scattering outgoing waves are imposed,

$$\mathbf{F}^{(+)\,Jp}(E;R) \underset{R\to\infty}{\longrightarrow} \mathbf{O}^{-\,Jp}(E;R) - \mathbf{O}^{+\,Jp}(E;R)\,\mathbf{S}^{Jp}(E)\,. \tag{17}$$

The symbols $\mathbf{O}^{\pm\,Jp}$ denote diagonal matrices built of Riccati-Hankel functions of order $\Lambda_{\bar{l}}$, see Ref. 25 for more details. The 'energy-normalization' of the scattering functions is assumed.

The reason for introducing the ro-vibrational adiabatic basis here is the expectation that the dimension M of the coupled equation problem (16) may substantially be reduced in comparison with the dimension N of the problem in the BF-diabatic basis, even if the CCr approximation is used. Obviously, having to solve smaller sets of the coupled equations in the adiabatic representation instead of the equations in the diabatic representation would not yet guarantee any substantial computational savings. Sharp structures due to avoided-crossings of the adiabatic potentials are likely to occur in the non-adiabatic couplings, see Fig. A2 in Ref. 55 and Fig. C5 in Ref. 27, and very small step size would be needed to pass them through in the course of solving the coupled equations. However, one has now at choice the Smooth-Variable Discretization (SVD) technique[30–32]. This technique avoids the usual difficulties with strongly localized non-adiabatic couplings at the expense of requiring somewhat larger amount of information on input. Namely, it requires that overlapping integrals between the adiabatic basis functions at neighboring R-points of a grid covering the range $R_0(\approx 0) - R_\infty(\to\infty)$ be available. This information is available here in terms of the matrices

$$\underset{M\times M}{\mathcal{O}^{Jp}}(R;\overline{R}) = [\mathbf{\Upsilon}^{Jp}(R)]^T\ \underset{N\times M}{\mathbf{\Upsilon}^{Jp}}(\overline{R})\,. \tag{18}$$

The SVD technique can be combined with the existing propagative methods of solving the coupled radial equations. Combinations with the renormalized Numerov-related propagators have been described in Ref. 31. In this work, like in Ref. 32, exploited are some algorithms derived from the log-derivative method[28], namely, the algorithms presented in Ref. 29 under the heading 'For equations in the quasi-diabatic representation'. Though originally designed to situations when only the nonadiabatic couplings $\mathbf{A}$ and $\mathbf{B}$ are available on input, these algorithms require merely a slight modification in order to work efficiently with the overlaps. In Part A of Supplementary Material, there are some details on the modified algorithms for evaluation of free-free and bound-free transition amplitudes (analytical proof of correctness, numerical tests of convergence properties) which are useful in the calculations of the resonance characteristics.

Within the close-coupling approach, the line strength $S_{\mathrm{i}\to\mathrm{f}}$ due to bound→resonance phototransition is obtained as

$$S_{\mathrm{i}\to\mathrm{f}} = \tfrac{\pi}{2}\Gamma \times \mathbf{T}^{\dagger}\mathbf{T}(E_{\mathrm{f}}^{\mathrm{res}} J_{\mathrm{f}} p_{\mathrm{f}}; E_{\mathrm{i}}^{B} J_{\mathrm{i}} p_{\mathrm{i}})\,, \tag{19}$$

where $\underset{N_{\mathrm{o}}\times 1}{\mathbf{T}}(E_{\mathrm{f}}^{\mathrm{res}} J_{\mathrm{f}} p_{\mathrm{f}}; E_{\mathrm{i}}^{B} J_{\mathrm{i}} p_{\mathrm{i}}) := \frac{\sqrt{2J_{\mathrm{f}}+1}}{C(J_{\mathrm{i}} 1 J_{\mathrm{f}}, M_{\mathrm{i}} q M_{\mathrm{f}})} \langle \mathbf{\Psi}^{(+)\,J_{\mathrm{f}} M_{\mathrm{f}} p_{\mathrm{f}}}(E{=}E_{\mathrm{f}}^{\mathrm{res}}) | d_q \Psi^{J_{\mathrm{i}} M_{\mathrm{i}} p_{\mathrm{i}}}(E_{\mathrm{i}}^{\mathrm{B}}) \rangle$ — the vector of reduced transition amplitudes to N_{o} open resonance decay channels is evaluated according to the formula[24,27,42]

$$\mathbf{T}(E_{\mathrm{f}}^{\mathrm{res}} J_{\mathrm{f}} p_{\mathrm{f}}; E_{\mathrm{i}}^{B} J_{\mathrm{i}} p_{\mathrm{i}}) = \mathbf{U}^{J_{\mathrm{f}} p_{\mathrm{f}}\,T} \left\langle {}_{\mathrm{BF}}\mathbf{F}^{(+)\,J_{\mathrm{f}} p_{\mathrm{f}}}(E_{\mathrm{f}}^{\mathrm{res}}) \right|_{\mathrm{BF}} \mathbf{d}^{J_{\mathrm{f}} p_{\mathrm{f}}, J_{\mathrm{i}} p_{\mathrm{i}}}\, {}_{\mathrm{BF}}\mathbf{F}^{J_{\mathrm{i}} p_{\mathrm{i}}}(E_{\mathrm{i}}^{B}) \rangle_R \tag{20}$$

with the matrix $\underset{N\times N}{{}_{\mathrm{BF}}\mathbf{d}^{J_{\mathrm{f}} p_{\mathrm{f}}, J_{\mathrm{i}} p_{\mathrm{i}}}}(R)$ containing the following elements

$$\left[{}_{\mathrm{BF}}\mathbf{d}^{J_{\mathrm{f}} p_{\mathrm{f}}, J_{\mathrm{i}} p_{\mathrm{i}}}(R)\right]_{v' j' \lambda',\, v j \lambda} = \tfrac{1+p_{\mathrm{f}} p_{\mathrm{i}} (-1)^{J_{\mathrm{f}}+J_{\mathrm{i}}+1}}{2} \sum_{\Lambda=-1}^{1} \sqrt{2J_{\mathrm{i}}+1}\, C(J_{\mathrm{i}} 1 J_{\mathrm{f}}, \lambda \Lambda \lambda')\, f_{\Lambda}^{\lambda} \left[\mathbf{d}_{\Lambda}^{\lambda}(R)\right]_{v' j', v j}\,, \tag{21}$$

where

$$\left[\mathbf{d}_{\Lambda}^{\lambda}(R)\right]_{v' j',\, v j} = \sum_{L} \langle v' j' | D_{L|\Lambda|}(r,R) | v j \rangle_r\, g_{L\Lambda}^{\lambda}(j', j)\,, \tag{22}$$

$$g_{L\Lambda}^{\lambda}(j', j) = (-1)^{L} \left[\tfrac{(L+|\Lambda|)!}{(L-|\Lambda|)!}\right]^{1/2} C(jLj', \lambda\, \Lambda\, \lambda{+}\Lambda)\, C(j'Lj, 000)\,, \tag{23}$$

$$f_{\Lambda}^{\lambda} = \left[1 + (1{-}\delta_{\Lambda,0})(1{-}\delta_{\lambda,0})(1{-}\delta_{\lambda+\Lambda,0})\right]^{-\frac{1}{2}}\,, \tag{24}$$

and the functions $D_{L|\Lambda|}(r,R)$ come from expansions of the two non-zero components of the dipole vector $\mathbf{d}(\mathbf{r},\mathbf{R})$ along the BF-axes into the Legendre polynomials and the associated functions: $d_Z(r,R,\theta){=}\sum_L D_{L0}(r,R)\, P_L(\cos\theta)$ and $d_X(r,R,\theta){=}\sum_L D_{L1}(r,R)\, P_L^1(\cos\theta)$.

III. CALCULATIONS

A. Methods

'Exact' (3D). This term signifies calculations performed with application of the theory outlined in the previous section. '3D' refers to the fact that all three modes of vibrational motion in the complexes, i.e. the r-, θ-, and R-motions, in all their bound and quasi-bound states are accounted for by the bases and the equations of the close-coupling approximation. The accuracy controlling parameters of this approximation, i.e. the values of $v_{\max}$, $j_{\max}$, and $\lambda_{\max}$ determining the BF-diabatic basis size, the range $[R_0, R_\infty]$ of integration of the coupled equations were adjusted to properties of state being determined. For calculations on $v_r{=}0,1$ states of the complexes, the bases were built of 28 diatomic $v\,j$ functions, with $v{=}0{-}3$ and j being even or odd integers from the $0{-}13$ range. For $v_r{=}3,4$ states, the values $v_{\max}{=}v_r{+}2$ and $j_{\max}{=}15,17$ were adopted. The parameter $\lambda_{\max}$ was usually chosen as $\max(4, b{+}2)$. Larger values of this parameter, up to $\lambda_{\max}{=}8$, were used in large J ($>$20) cases, especially in calculations of partial widths. The coupled equations were integrated from $R_0{=}0.5\mathring{A}$ up to maximally $R_\infty{=}40\mathring{A}$. The boundary R_∞ could be shifted towards origin, even by $25{-}20\mathring{A}$, in calculations on bound states with low values of the number v_R. The bound-state energies and functions were determined with the help of the artificial-channel log-derivative propagation method[33]. In calculations on the quasi-bound states, the SF-adiabatic representation of the coupled equations was exploited. The energies and widths of these states were determined via evaluation and analysis of the life-time matrices using the SVD verions of the log-derivative algorithms for first- and second-order free-free transition amplitudes presented in Ref. 55. Due to faster convergence with respect to the adiabatic basis size and due to properties of the SVD technique (constant step size, practically the same as in the diabatic representation), all the quasi-bound calculations could be substantially (about eight times) speeded up.

Perturbative (3D-CM). These calculations were performed in connection with the vibrational predissociation (VP) in the complexes which is driven by relatively weak coupling between the internal (r) and intermolecular vibrational (R and θ) modes of motion. By treating this coupling as perturbation it became more easy to rationalize some features of the VP which were displayed by results of the 'exact' calculations. More specifically, the bound-continuum configuration-mixing (CM) theory[34] was applied to the coupled equations in the BF-diabatic representation. For a given predissociating state with $v_r>0$, the P (continuum)- and the Q (bound) -subspaces were chosen as spanned by the basis functions with v changing from 0 to v_r-1 and from v_r to v_r+2, respectively. 0-th order approximation to energy of the state, $E^{(0)Jp}$, was obtained as energy of a related state in the Q-subspace, $[\mathbf{H}^{Jp}_{QQ}-E^{(0)Jp}\mathbf{I}_{QQ}]\mathbf{F}^{Jp}_{Q}=0$, and the 2-nd order approximation, $E^{\mathrm{CM}Jp}$, as the sum $E^{(0)Jp}+E^{\mathrm{shft}Jp}$. The values of $E^{\mathrm{shft}Jp}$ and $-\frac{1}{2}\Gamma^{\mathrm{CM}Jp}$ were obtained as real and imaginary parts, respectively, of the scalar product $\langle\mathbf{F}^{Jp}_{Q}|\mathbf{H}^{Jp}_{QP}\,\mathbf{f}^{(+)Jp}_{P}(E)\rangle$ with the vector of radial functions $\mathbf{f}^{(+)Jp}_{P}(E;R)$ at $E=E^{\mathrm{CM}Jp}$ describing the final stage of the VP process, i.e. the half-collision in the P- subspace. Precisely, $\mathbf{f}^{(+)Jp}_{P}(E;R)$ is the solution of the driven coupled equations, $[E\mathbf{I}_{PP}-\mathbf{H}^{Jp}_{PP}]\,\mathbf{f}^{Jp}_{P}=\mathbf{H}^{Jp}_{PQ}\,\mathbf{F}^{Jp}_{Q}$, which vanishes at $R=0$ and behaves as $-\mathbf{O}^{+Jp}(E;R)\,\mathbf{t}^{Jp}(E)$ at $R\to\infty$. (The index 'BF' of the blocks of the Hamiltonian matrix and of the radial functions are omitted here for clarity.) The partial widths were obtained as $\Gamma^{\mathrm{CM}Jp}_{vj}=\frac{1}{2\pi}\sum_{l}|t^{Jp}_{vjl}(E^{\mathrm{CM}Jp})|^2$. Three, four iterations over the energy, starting from $E=E^{(0)Jp}$, were usually performed to get converged values of $E^{\mathrm{shft}Jp}$ and of all $\Gamma^{\mathrm{CM}Jp}_{vj}$s up to five significant figures. Obviously, solving of the driven coupled equation problem could be avoided if the level shift $E^{\mathrm{shft}Jp}$ were negligible or uninteresting. In such cases, it would suffice to exploit the relation of the vector $\mathbf{t}^{Jp}(E)$ to the radial component matrix $\mathbf{F}^{(+)Jp,vjl}_{P}(E;R)$ of the full scattering function in the P-subspace, $t^{Jp}_{vjl}(E)=-2\pi\imath\langle\mathbf{F}^{Jp}_{Q}|\mathbf{H}^{Jp}_{QP}\,\mathbf{F}^{(+)Jp,vjl}_{P}(E)\rangle$. One should note that this relation at $E=E^{(0)Jp}$ is actually exploited in the 'Diabatic Vibrational Golden Rule' approaches[35–37], see also Table DI in Ref. 55.

Of the radial functions $\mathbf{f}^{Jp}_{P}(E;R)$ and $\mathbf{F}^{(+)Jp}_{P}(E;R)$ combined appropriately with the BF-basis functions, one can construct coordinate dependent counterparts $X(R,\theta)$ of the characteristics $X=E^{\mathrm{CM}Jp}$, $\Gamma^{\mathrm{CM}Jp}$, $\Gamma^{\mathrm{CM}Jp}_{vj}$ such that $X=\int dR\int\sin\theta\,d\theta\,X(R,\theta)$, see Eqs. D1–19 in Ref. 55. The coordinate-dependent level shifts and widths were constructed for a number of $J=0$ resonances in order to get a better insight into the role of rovibrational excitations in the Q-subspace, influencing the resonance decay through the driving term to the coupled equations, and into the role of inelastic rotational transitions during separation of the fragments in the P-subspace.

2D approximate. In these calculations, the diatomic vibrational (r) motion was diabatically separated from the other modes of motion in the complexes. This means that the BF-diabatic bases used in formulation of the close-coupling equations were restricted to include a single v-state only. By this restriction, the vibrationally predissociationg states of the complexes, i.e. states assigned with $v_r\geq1$, become approximated by bound states of the Hamiltonian matrix built of the $v=v_r$ basis states. This 2D approximation was exploited in nearly all theoretical simulations of rotationally resolved spectra of the complexes formed by the $H_2(D_2)$ molecules with metallic cations (M^+) which have been investigated experimentally thus far[1,2]. However, accuracy of the approximation was not quite certain[38] as it could be quantified only in application to truly bound states ($v_r=0$). Because of this uncertainty, less information could be inferred from the simulations on quality of the used PESs. In this work, it was possible to test the 2D approximation against the 3D 'exact' and the 3D-CM approaches on any state of the studied complexes.

B. Electronic structure input

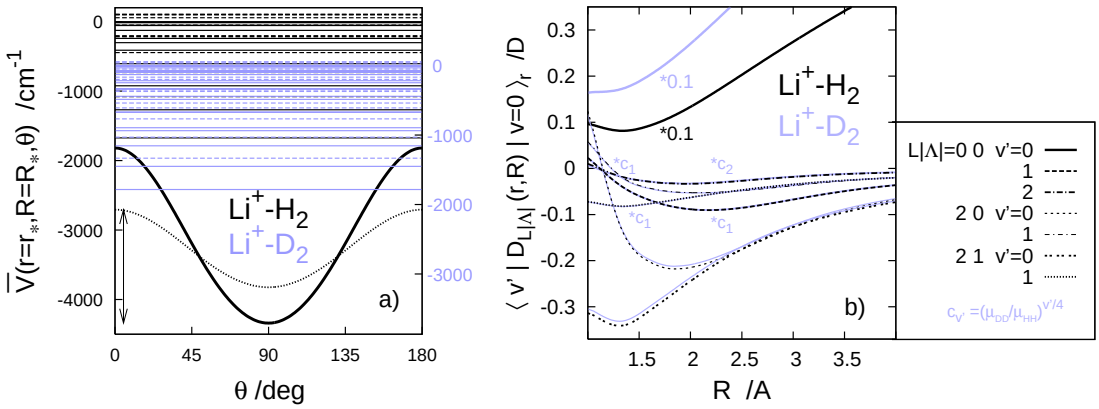

Fig. 1. The electronic structure input to the present calculations, taken from Ref. 8.
a) $\overline{V}(r,R,\theta)$ — the PES of the ground electronic states of the $[LiH_2]^+$ system. 1D cuts through the minimum, r_*=0.7503Å, R_*=1.9870Å (thick line), and the saddle point at θ=0, π, r_*=0.7428Å, R_*=2.4073Å. Shown are also the energy levels of bound J=0 states of the complexes Li^+–para-H_2, Li^+–ortho-H_2, Li^+–ortho-D_2, Li^+–para-D_2 (black solid, dashed, blue solid, and dashed lines, respectively). The dissociation thresholds Li^++$a_2(v{=}0j{=}0)$ of the complexes with a=H and a=D, at which E is set to zero, lie 4339.9 and 3706.4 cm^{-1}, respectively, above the minimum of the PES, and 2183.3 and 1549.8 cm^{-1} above the asymptote of the PES. The respective thresholds v=0 j=1 lie 118.5 and 59.8 cm^{-1} higher. The zero-point energies of Li^+–H_2 and Li^+–D_2 are 2665.2 and 1922.8 cm^{-1}, respectively. All levels lie above the barrier to linearity, of 1633 cm^{-1}, which is marked by the double arrow.
b) The components of the electric dipole vector field of the ground state of $[LiHH]^+$ along the body-fixed Z- and X-axes with the origin at the center-of-mass of the Li^+–H_2 complex, represented by the expansions $d_Z(r,R,\theta)=\sum_{L=0,2} D_{L0}(r,R)P_L(\cos\theta)$ and $d_X{=}D_{21}(r,R)P_2^1(\cos\theta)$ with $D_{00}(r,R)\to\frac{2m_H}{m_{Li^+}+2m_H}Re$ and $D_{2|\Lambda|}(r,R)\to 0$ for $R\to\infty$. Matrix elements of the strength functions $D_{L|\Lambda|}(r,R)$ between vibrational states (v=0, j=0 and $v',j'{=}L$) of H_2 and D_2 molecules. The matrix elements $\langle v'|\ldots|0\rangle_r$ for D_2 with v'=1, 2 are almost indistinguishable from their counterparts for H_2 in result of multiplication by the specified mass factors. The elements $\langle 0|\ D_{00}|0\rangle_r$ of the two complexes differ because of the center-of-mass shift, $D_{00}^{Li^+-D_2}=D_{00}+\left(\frac{\mu_{Li^+-HH}}{2m_H}-\frac{\mu_{Li^+-DD}}{2m_D}\right)Re$. Note that these elements are diminished 10 times in the figure.

The input needed is taken from Ref. 8. It is the PES of the ground electronic states of the $[LiH_2]^+$ system which is resolved into the Li^+–H_2 interaction and the diatomic H–H potentials, $\overline{V}(r,R,\theta){=}V(r,R,\theta){+}\overline{V}_\infty(r)$ with $\overline{V}_\infty(r){:=}\lim_{R\to\infty}\overline{V}(r,R,\theta)$, and the dipole moment surfaces $d_Z(r,R,\theta)$ and $d_X(r,R,\theta)$. Some characteristics of these surfaces are presented in Fig. 1. In particular, information is provided on the zero-point energies (ZPE) and the positions of two lowest dissociation limits of the complexes Li^+–H_2 (D_2) on the surface $\overline{V}(r,R,\theta)$. Worth of noting seems the fact that the present values of ZPE(Li^+–a_2) for a=H and a=D differ by only −14.2 and +4.8 cm^{-1}, respectively, from the values resulting from the PES used in Refs. 9 and 10. The dissociation energies $D_0(Li^+{-}a_2)$ are larger by only 8.3 and ∼9.7 cm^{-1}, see Ref. 39. The two other PESs important in the discussion of the present results are those published in Ref. 6 and in Ref. 5, respectively. In comparison with the former PES, the binding characteristics of the PES used here differ rather significantly[40]: the ZPEs and the D_0s of the Li^+–H_2 (D_2) complexes are smaller by as much as 90.1 (∼60) and 57.6 (∼87) cm^{-1}, respectively. In comparison with the latter PES, these characteristics differ about two times less: the ZPEs are smaller by 53.2 (38.6) and the D_0s are larger by 28.0 (32.4) cm^{-1}.

The positions of the lowest dissociation limits of the complexes relative to the asymptote of the PES, i.e the ZPEs of the monomers H_2 (D_2) in the potential $\overline{V}_\infty$, are too high by 2.87 (2.97) cm^{-1} as compared to positions in accurate Born-Oppenheimer potential for H_2, see Fig. B1 (Ref. 55). Distances to higher limits resulting from this potential, $\varepsilon_{v,j}{-}\varepsilon_{00}$, are

in turn too small. The shifts are tiny for j=1, of $-0.09\,(-0.04)$ cm^{-1}, but increase with growing j and v, reaching values of $-0.28\,(-0.13)$, $-4.83\,(-0.28)$ and $-18.3\,(-4.45)$ cm^{-1} cm^{-1} for $(v\,j)$=(0 2), (1 0), and (2 0), respectively. More details are given in Tables BI–II and Fig. B1.

In all calculations of this paper the nuclear masses were used: m_p=1836.152701 m_e, m_d=3670.48305 m_e, and $m_{^7\mathrm{Li}}$=12786.3931 m_e.

IV. RESULTS. DISCUSSION

The list of dynamical and spectral characteristics of the Li^+–H_2 (D_2) complexes determined in the calculations includes:

(i) the energies E_n^{B} of all bound states; 1233 (3503) such states have been found below the lowest dissociation thresholds of the complexes[41], v=0 j=0 and v=0 j=1 for Li^+–pH_2 (oD_2) and Li^+–oH_2 (pD_2), respectively,

(ii) the energies E_n^{res} and the dissociative widths Γ_n of about 3900 (2100) quasibound states; about 1400 (1900) of these states decay predominantly by the VP mechanism,

(iii) the populations of decay channels $P_{n,vj}$ in the VP of about 180 (120) states,

(iv) the TIPSes Z(T) for temperature range up to 400 K,

(v) the frequencies $\nu_{\mathrm{i}\to\mathrm{f}}$, the strengths $S_{\mathrm{i}\to\mathrm{f}}$, and the absolute intensities $I_{\mathrm{i}\to\mathrm{f}}(T)$ at T=296 K of about 9200 (12100) rovibrational transitions i→f belonging to 19 (13) vibrational absorption bands $[0\,v''_\theta\,v''_R]\to[v'_r\,v'_\theta\,v'_R]$ in the near-infrared (v'_r=1, 2) and to 14 (14) bands in the far- and mid-infrared ranges (v'_r=0);

(v)' the integrated intensities $I_{[\mathrm{v}n]\to[\mathrm{v}']}$ of 16 bands of each complex for T up to 330 K, and

(vi) the absorption cross-sections $\sigma(\nu; 296\,K)$ in several frequency intervals, embracing lines $\sigma_{\mathrm{i}\to\mathrm{f}}$ from 13 (12) vibrational bands. The line shapes are described by the Voigt profiles $V(\nu-\nu_{\mathrm{if}};\gamma,\alpha)$ with the parameter α of the Gaussian component $G_\alpha(\nu)=\frac{\alpha}{\sqrt{\pi}}\exp(-\alpha^2\nu^2)$ fixed to the value suggested in the experimental work[3], i.e. $\alpha=2\sqrt{\ln 2}/(0.017\,\mathrm{cm}^{-1})$.

In the majority, the determined energy levels/states of the two complexes are fully assigned, albeit sometimes very approximately, with the quantum numbers defined in Sec. IIA. So, they can be categorized as belonging to 106 (116) different vibrational states $[v_r\,v_\theta\,v_R]$ (with v_r, v_θ and v_R ranging up to 3, 5 (7), and 10 (12), respectively) and to 317 (404) rovibrational groups $[v_r\,v_\theta\,v_R]\,k$, or $(v_r\,b\,k\,v_R)$. The lowest (J^p=k) levels of nearly all of the groups in $v_r=0,1$ states are shown in Figs. 2 (3). In numerical form, information on positions and widths of these levels is provided in Tables BI–BII, DI (CI–CII, DII). Sequences of higher (J^p>k) rotational levels have been actually determined in only 183 (161) k-groups within 53 (44) vibrational states. Of them, 55 (119) groups, with maximal J-value of 27 (36), belonging to 22 (35) states $[v_r$=0 $v_\theta\,v_R]$ are the bound levels and 34 (42) groups within 10 (9) states $[v_r$=1−2 $v_\theta\,v_R]$ are the quasi-bound VP levels. Detailed information on the latter levels and on the groups of bound levels which were included in the line strength calculations is provided in Tables BIV–BV (CIII–CIV). About 2700 (450) of the levels determined and assigned with v_r=0 lie above the lowest dissociation thresholds of the complexes. The levels of Li^+–H_2 were exploited in the present study to test convergence of the calculated TIPS for this complex Much greater is, however, the role of these (predominantly) unstable levels in dynamics of the radiative association reaction $Li^+ + H_2 \to LiH_2^+ + h\nu$, a study of which will be described elsewhere.

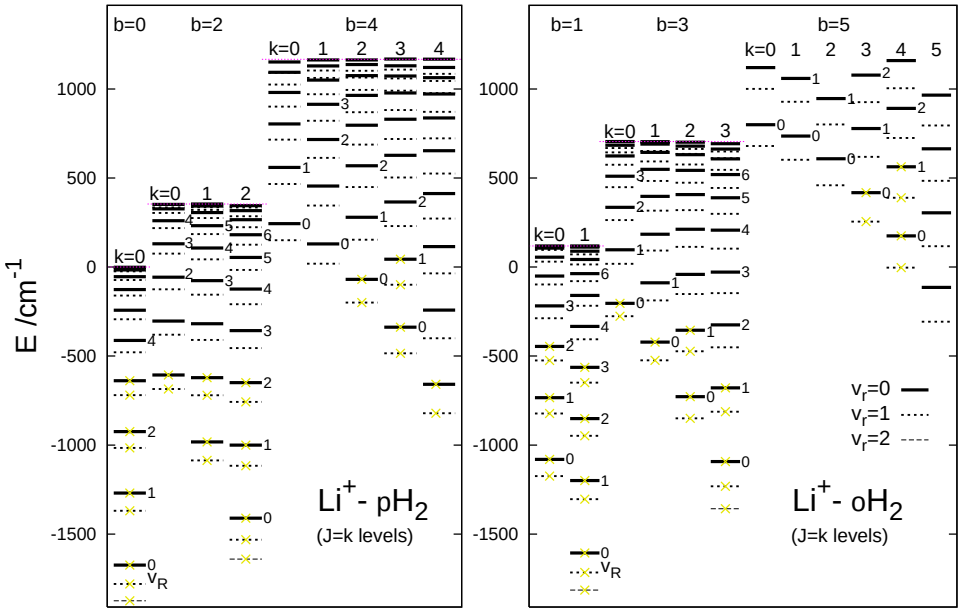

Fig. 2. The structure of $J{=}k$ energy levels of the Li^+–H_2 complex associated with the $v{=}0\, j{=}0,\ldots,5$ and $v{=}1\, j{=}0,\ldots,5$ thresholds (continuous and dotted lines, respectively). Shown are also the lowest levels associated with the $v{=}2\, j{=}0,1,2$ thresholds (dashed lines). The $v{=}0\, j$ thresholds are shown with the red dotted lines. The thresholds $v{>}0\, j$ are shifted down so that $v{=}1\, j{=}0$ and $v{=}2\, j{=}0$ coincide with $v{=}0\, j{=}0$. Each line in $k{>}0$ ladders represents two, e- and f-parity, states. The yellow crosses are to inform that transitions to or from these levels and sets of $J^p{>}k$ levels in the same groups $(v_r\, b\, k\, v_R)$ were included into the simulations of the absorption spectrum of the complex carried out in this work, presented in Figs. 13, 17–18, B5–B6 and in Tables XII–XIII, BVIII–BXI.

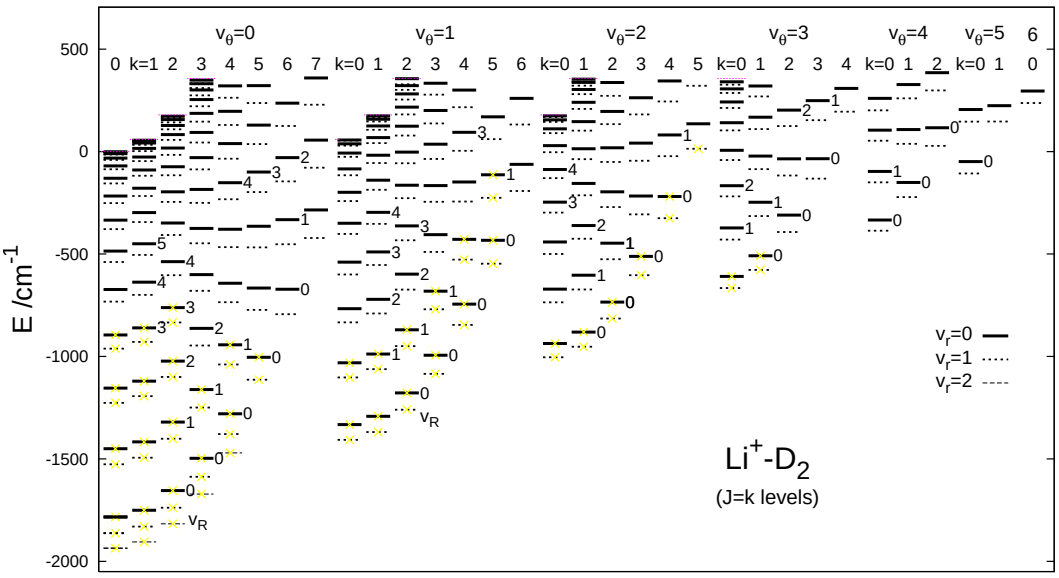

Fig. 3 Same as in Fig. 2 for Li^+–D_2 except the number v_θ $(=b{-}k)$ instead of b is used to arrange the k-ladders of levels. It should be noted that in the present complex, unlike in the Li^+–H_2, several levels associated with $j{=}6$ and $j{=}7$ thresholds fall into the energy ranges below the respective $v\, j{=}0$ limits. The yellow crosses indicate the vibrational states $[v_r\, v_\theta\, v_R]$ and the groups k of their rotational $J{\geq}k$ levels which were used in the simulations of the absorption spectrum presented in Figs. 14, C3, C7 (and in Tables CXIII–CXVI) and/or in the calculations of the integrated band intensities presented in Table XII (and in Fig. C9).

TABLE I: Li^+–$H_2(D_2)$. Harmonic frequencies ω_m of vibrational modes m=r, θ, R and anharmonic constants $x_{mm'}$ (all in cm^{-1}) from least-squares fits to the formula for semirigid asymmetric tops, Eq. (25). Comparison with results of Ref. 5 in terms of relative deviations $[X(\text{Ref. } 5)/X-1]\times 100\%$ for X=$\omega_m, x_{mm'}$, shown within $\lfloor\ \rfloor$.

	ω_r	ω_θ	ω_R	x_{rr}	$x_{\theta\theta}$	x_{RR}	$x_{r\theta}$	x_{rR}	$x_{\theta R}$	σ^a
Li^+–H_2	4267(5)[b]	710(5)	477(5)	−115(2)	−53(2)	−28(1)	15(2)	9(2)	−51(2)	2
	⌊2.67⌋	⌊−1.1⌋	⌊−2.5⌋	⌊−8.7⌋	⌊5.7⌋	⌊−3.6⌋	⌊88⌋	⌊−11⌋	⌊−7.8⌋	
Li^+–D_2	3024(3)	512(3)	377(3)	−59(1)	−27(1)	−17(1)	7(1)	5(1)	−30(1)	1
	⌊2.61⌋	⌊−0.9⌋	⌊−0.8⌋	⌊−8.5⌋	⌊3.7⌋	⌊5.9⌋	⌊129⌋	⌊0.0⌋	⌊0.0⌋	

[a]Root mean square errors of the fits. For each complex, energies of (18) states with v_r=0−2, v_θ=0−2, and $v_r+v_\theta+v_R\leq 3$ were used; the same set of states was used in the fits of Ref. 5.

[b]In parentheses are the calculated uncertainties of the constants.

A. VIBRATIONAL ENERGY LEVELS

Confining considerations to low excited (by no more than three quanta) vibrational states, one may attempt to describe their energies with the following formula, appropriate for near-rigid asymmetric top molecules[44]

$$G(v_1,v_2,v_3)=\sum_{m=1}^{3}\omega_m(v_m+\tfrac{1}{2})+\sum_{m=1}^{3}\sum_{m'=m}^{3}x_{mm'}(v_m+\tfrac{1}{2})(v_{m'}+\tfrac{1}{2})\,; \qquad (25)$$

$G(v_1,v_2,v_3)$ denotes here energy of state $[v_r\, v_\theta\, v_R]\ J$=0 relative to the minimun of the PES. The parameters of this formula, the harmonic frequencies ω_m and the anharmonic constants $x_{mm'}$, are among the characteristics of the (20) vibrational states of (each of) the Li^+–$H_2(D_2$, $T_2)$ complexes which have been studied in Ref. 5.

In Table I, it is demonstrated what changes of these characteristics are induced by the PES used in the present study. According to the listed relative deviations, the only severe changes occur in the case of the parameter $x_{r\theta}$ which describes the coupling between the r- and θ-motions in the complexes. Considering the sizes of the parameters, one should also state that the present frequencies ω_r are changed (improved) by quite substantial amounts. However, the changes in the frequencies ω_m and the anharmonic constants $x_{m\,m}$ of the intermolecular modes m=θ and m=R look reasonably small. As a matter of fact, they are, on average, about 20 times smaller than the deviations observed in the analogous comparisons with results from the two other previously used PESs[7,9], presented in Table BIII (Ref. 55).

In Table II, the calculated values of vibrational transition frequencies in the Li^+–$H_2(D_2)$ complexes are presented. Fundamental and two overtone transitions in the intramolecular (r) mode are included. Their frequencies are listed together with the redshifts from the respective accurate $Q_v(0)$ transition frequencies in free H_2 (D_2). The values of the redshifts obtained for the v_r=0→1 transitions in the two complexes are 108.1 (78.2) cm^{-1} and compare favorably with the experimental values[3,4]: absolute deviations are only 0.3 (−0.8) cm^{-1}. The redshifts obtained for the v_r=0→2 and v_r=0→3 transitions are bigger by factors of 2.0 (2.0) and 2.9 (3.0), respectively. This increase is in full agreement with one of the conclusions of the analysis performed in Ref. 46. As to the intermolecular modes, shown are frequencies of two lowest transitions, (ν_θ, $2\nu_\theta$) and (ν_R, $2\nu_R$), in the complexes with the diatoms in the v=0−3 states. Relations between these frequencies are, at the most, qualitatively consistent with formula (25). For example, the differences $\nu_R(v+1)-\nu_R(v)$ for v=0, 1, 2 are nearly independent of v, as they should if $\nu_R(v)\approx G(v,0,1)-G(v,0,0)$, but their values are almost 2 times larger than the values of the parameter x_{rR} listed in Table I.

TABLE II: Li^+–$H_2(D_2)$. Fundamental and two overtone transitions frequencies in monomer vibrations (ν_r), shifts ($\Delta\nu$) from $Q_v(0)$ transition frequencies in free $H_2(D_2)$[a], fundamental and first overtone transition frequencies in intermolecular stretching (ν_R) and bending (ν_θ) vibrations within the complexes with $H_2(D_2)$ in v=0−3 states. Accuracy of 2D and 3D-CM approximations: in angle brackets — deviations of 2D results from the 3D 'exact' results, below them — the respective deviations of CM results. Comparison with frequencies obtained from three other PESs: from the PES of Ref. 5 — within ⌊ ⌋, from the PES of Ref. 6, calculated in Refs. 7 and 3 — in square brackets, and from the PES of Ref. 9 — in braces. Listed are absolute deviations of these frequencies from the present 'exact' values. All entries are in cm^{-1}.

	v	ν_r	$\Delta\nu$[a]	ν_θ	$2\nu_\theta$[b]	ν_R	$2\nu_R$
Li^+–H_2	0	0		594.33 ⟨−3.44⟩	1068.18 ⟨−5.15⟩	405.15 ⟨−1.14⟩	750.36 ⟨−2.48⟩
		/ −1674.61[c] ⟨ 8.85⟩/		⌊−5.8⌋	⌊−18.5⌋	⌊−6.1⌋	⌊−13.5⌋
				[52.3]	[51.6]	[21.0]	[7.8]
	1	4053.10 ⟨−0.60⟩	−108.07[d]	605.42 ⟨−4.51⟩	1094.77 ⟨−6.05⟩	410.55 ⟨−1.12⟩	763.99 ⟨−2.39⟩
		⌊141.7⌋ 0.01		⌊9.9⌋ 0.01	⌊6.7⌋ 0.01	⌊−6.1⌋ 0.00	⌊−14.1⌋ 0.01
		[−0.2][e]				[19.6][e]	[12.3][e]
	2	7872.46 ⟨−2.11⟩	−214.54	615.59 ⟨−5.74⟩	1118.53 ⟨−6.81⟩	415.10 ⟨−1.12⟩	775.43 ⟨−2.29⟩
		⌊303.6⌋ 0.03		⌊23.5⌋ 0.03	0.09	⌊−6.9⌋ 0.00	0.02
		[−21.4][e]				[24.5][e]	[25.7][e]
	3	11470.94 ⟨−4.29⟩	−311.45	625.24 ⟨−7.11⟩	1140.00 ⟨−7.74⟩	419.15 ⟨−1.20⟩	785.41 ⟨−2.28⟩
		0.09		0.09	0.20	0.00	0.03
Li^+–D_2	0	0		451.29 ⟨−2.72⟩	846.75 ⟨−4.51⟩	333.14 ⟨−0.88⟩	629.34 ⟨−1.91⟩
		/ −1783.61[c] ⟨ 9.44⟩/		⌊−4.1⌋	⌊−10.8⌋	⌊−3.3⌋	⌊−9.2⌋
				[51.7]		[31.9]	
				{35.0}	{160.9}	{24.5}	{92.7}
	1	2915.45 ⟨−0.05⟩	−78.17[d]	455.63 ⟨−3.51⟩	858.56 ⟨−5.55⟩	335.90 ⟨−0.88⟩	636.07 ⟨−1.91⟩
		⌊94.8⌋ 0.01		⌊4.9⌋ 0.00	⌊5.4⌋ 0.01	⌊−3.9⌋ −0.00	⌊−9.8⌋ −0.00
		{2.1}					
	2	5710.22 ⟨−0.57⟩	−157.90	459.87 ⟨−4.37⟩	869.43 ⟨−6.64⟩	338.35 ⟨−0.89⟩	642.05 ⟨−1.90⟩
		⌊200.5⌋ 0.04		⌊13.4⌋ 0.01	0.03	⌊−3.8⌋ −0.00	−0.00
	3	8390.49 ⟨−1.49⟩	−235.11	464.15 ⟨−5.32⟩	879.62 ⟨−7.85⟩	340.56 ⟨−0.92⟩	647.43 ⟨−1.90⟩
		0.09		0.03	0.06	−0.01	−0.00

[a]Theoretical values[54] are taken for the transition frequencies in free H_2 and D_2.

[b]Obtained as $E([v_r{=}v\, v_\theta{=}2\, v_R{=}0]\, J{=}0) - E([v_r{=}v\, 0\, 0]\, J{=}0)$ and the ν's concerning the R- and θ-vibrations are obtained analogously.

[c]The energy of the ground state of the complex relative to the v=0 j=0 threshold, $E([0\,0\,0]\, J{=}0)$, from the present 'exact' calculations. 2D result for this energy is shifted up by amount shown in the angle brackets.

[d]The experimental values (Refs. 3,4) are −107.8 and −79.0 cm^{-1} for Li^+–H_2 and Li^+–D_2, respectively.

[e]Deduced from the resonance energies listed in Table 2 of Ref. 7 assuming that: i) these energies pertain to v_R=0−2 states associated with the thresholds v=1–2 j=0, i.e. not with odd j thresholds as communicated in the caption, ii) these energies are given relative to the asymptote of the PES, i.e. differently than the bound state energies in Table 1 which are relative to the $H_2(v{=}0\, j{=}0)$+Li^+ dissociation threshold, and iii) the included ZPE of H_2 has the value of 2180.87 cm^{-1} shown in Fig. 1. Only with the present assignment of the resonances of Ref. 7, the energy differences between them become reasonably consistent with the transition frequencies obtained here and (for R-mode) in Ref. 5.

Table II provides also information on accuracy of the two approximate 2D and 3D-CM approaches in the determination of the vibrational transition frequencies. The accuracy is of particular interest in cases involving predissociating states. The 3D-CM results are practically exact in all such cases shown. The 2D results are all too small by amounts varying from 0.6 (0.05) cm^{-1} for the fundamental transitions in the r-mode to about 4 (1.5) cm^{-1} for the second overtone in this mode, and above 7 (5) cm^{-1} for the hot v_r+v_θ=3+0→3+1 transitions. The errors of the v_r=0→1 transition frequencies look small. However, since the 3D 'exact' and CM results agree with the experimental data

within 1 cm^{-1}, the additional error of 0.6 cm^{-1} would alter rather significantly the assessment of accuracy of the used PES. Concerning the intermolecular modes, it is demonstrated in Table II that the 2D−3D deviations of the frequencies ν_θ and ν_R are comparable in size with the differences between the present values of these frequencies and the values obtained in Ref. 5, from certainly less accurate PES. This fact and an inspection of errors of 2D results for energies of a wider selection of $[v_r\, v_\theta\, v_R]$ states of the complexes, plotted in Fig. B2, leave no doubts that vibrational transition frequencies generated within the 2D approximation cannot be safely used in quantitative comparisons with accurate measurements from which conclusions on quality of PESs may be drawn.

B. ROTATIONAL ENERGY LEVELS in different vibrational states

Rotational structure in [0 0 0] and [1 0 0] states. Calculations versus experiment.

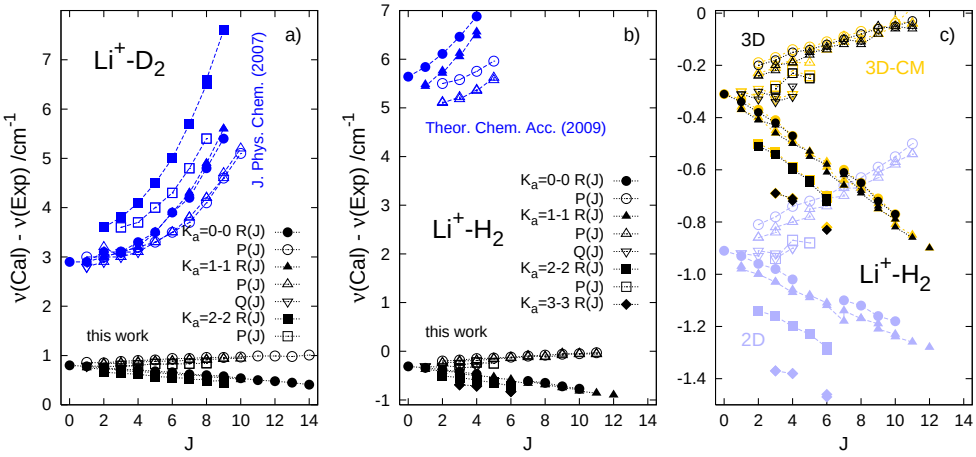

Fig. 4. Transition frequencies in v_r=0→1 bands of absorption spectra of the Li^+–H_2 and Li^+–D_2 complexes.

a)- b) Deviations of the values calculated in this and in the previous works, Refs. 9 and 10, from the values measured in Refs. 3 and 4. Deviations concerning transitions in the K_a>0 subbands from the initial J_{K_a,K_c} levels of *e*- and of *f*- parity (K_c equal to $J-K_a+\frac{1-(-1)^{K_a}}{2}$ and $J-K_a+\frac{1+(-1)^{K_a}}{2}$, respectively), barely distinguishable on the scale of the figure, are shown with the same symbols. See Fig. 5.

c) Comparison with the experimental data of three sets of theoretical results, obtained within the three approaches to dynamics of the complexes described in Sec. IIIA.

In Fig. 4 the confrontation is made on transitions between $(k\, J\, p)$ levels of these states, more specifically, on the frequencies of $R(J^p)$, $P(J^p)$, and $Q(J^p)$ transitions in the K_a=0−0, 1−1, 2−2, and 3−3 subbands of the v_r=0→1 band of the absorption spectrum. All the measured (93) frequencies of such transitions in the spectrum of the Li^+–H_2 complex[4] and all but one of the (105) *ro-vibrational transition frequencies* measured in the spectrum of the Li^+–D_2 complex[3] are reproduced by the present calculations with absolute deviations smaller than 1 cm^{-1}. The improvement over the previous calculations[9,10] is evident: the deviations are reduced by factors ranging from above 3 to above 40, see Tables BVIII and CXIV. As a matter of fact, no better agreement has been achieved thus far in any other theoretical simulation of the data provided by the infrared photodissociation spectroscopy experiments on M^+–$H_2(D_2)$ complexes[1,2].

As demonstrated in Fig. 4c, not only the accuracy of the used PES but also the 3D treatment of dynamics of the present complexes had a role in achieving the sub-cm^{-1} consistency with the measured transition frequencies. The use of the 2D approximation

would give the entire band in the spectrum of Li^+–H_2 shifted by ca -0.6 cm^{-1} and would also cause some slight changes in the relative positions of the subbands.

It is customary to represent the rotational energies in terms of *rotational and centrifugal distortion constants*. Sets of such constants have been extracted from the measured transition frequencies[3,4] by fitting the rotational levels in the initial and final vibrational states of the transitions to eigenvalues of the A-reduced Watson's Hamiltonian (Ref. 45). Full version of this Hamiltonian in the quartic approximation reads

$$\begin{aligned} H &= \tfrac{1}{2}(B+C)\mathbf{J}^2 + \left(A-\tfrac{B+C}{2}\right)J_z^2 + \tfrac{B-C}{2}J_{xy}^2 \\ &- \Delta_J\mathbf{J}^4 - 2\delta_J\mathbf{J}^2J_{xy}^2 - \Delta_{JK}\mathbf{J}^2J_z^2 - \Delta_K J_z^4 - \delta_K[J_z^2, J_{xy}^2]_+ , \end{aligned} \tag{26}$$

where $J_{xy}^2{:=}J_x^2-J_y^2$ and $[X,Y]_+{:=}XY+YX$. In the actual fits, some of the quartic terms were omitted. To compare with the parameters resulting from those fits, the calculated rovibrational energies, here and in the previous works[7,9,10], have been modeled analogously. Results are presented in Tables III–VI, BVI, and CVI.

The main fact documented in these tables is that the parameters of Hamiltonian (26) extracted from energies of the present calculations are best consistent with the experimental values; the rotational constants $\overline{B}^{\epsilon}{=}(B^{\epsilon}+C^{\epsilon})/2$ with $\epsilon{=}\prime\prime$ and $\epsilon{=}\prime$ for states [0 0 0] and [1 0 0], respectively, deviate from the experimental values by -0.6 to -0.8%. One may note that the rotational constants extracted from the energies of the Li^+–D_2 complex calculated in Ref. 9 are similarly close or even closer to the experiment. Unfavorable for these results is, however, the fact that the deviations 'Cal/Exp-1' of the constants $\overline{B}'$ differ so much, i.e. by 0.8–1.5%, from the deviations of their counterparts $\overline{B}''$. This causes the rapid growth with increasing number J of the discrepancy between the calculated and measured transition frequencies which is demonstrated by the blue curves in Fig. 4a.

$K{=}1$ *doubling.* An important feature of the rotational structures of the complexes, displayed by the spectra recorded in Refs. 3–4, is the splitting of lines in the $K_a{=}1$–1 subbands. Since determined by the small asymmetries $B''{-}C''$ and $B'{-}C'$ it is harder to reproduce in calculations than the Bs and Cs themselves. Fig. 5 shows what the calculations have actually given to compare with the (55) splitting values measured in the R-, P-, and Q-branches. Except for a few cases in the spectrum of Li^+–D_2, of $R(1)$, $P(2)$, $P(3)$, and $Q(1)$ lines, the present calculations reproduce the experimental data within ±4%. The previous calculations[9,10] were generally less successful, giving splitting even qualitatively inconsistent with the data for the R-branch in Li^+–D_2.

The splitting of $Q(J^f)$ and $Q(J^e)$ lines has been measured for a few lowest J values, $J{<}4$. Together with the splitting measured in the R- and P- branches, this enabled the experimentalists to provide some information on the $K{=}1$ doubling, $\Delta([v_r\, v_\theta\, v_R], J){=}E([v_r\, v_\theta\, v_R]\, k{=}1, J^f){-}E([\ldots]\, k{=}1, J^e)$, in each individual vibrational state, [0 0 0] and [1 0 0]. In Tables V and VI, the calculations are confronted with this information. Included are the calculated data for states [1 0 0] of the complexes and thereby the present confrontation completes those given in Tables III of Refs. 3 and 4. The assessment of the PES of Ref. 8, as enabling the most realistic description of the rotational structures in the two vibrational states, is confirmed.

Summarizing, the contents of tables and figures described in this subsection should give the reader a ground for believing that calculations on other vibrational states of the complexes using the same PES and the 3D treatment of dynamics will provide useful predictions for future experiments.

TABLE III: Infrared spectrum of Li^+–D_2. The v_r=0→1 band. Origins of K_a=0–0, 1–1, and 2–2 subbands (ν_0) and rotational constants[a] in [0 0 0] and [1 0 0] vibrational states (all in cm^{-1}). Comparison of calculated and experimental[b] data.

				Cal− Exp		
	$K_a=0$	$K_a=1$	$K_a=2$	$K_a=0$	$K_a=1$	$K_a=2$
ν_0	2915.445[c]	2914.155	2910.339	0.822 {2.94}[d]	0.796 {2.83}	0.753 {3.36}
					(Cal/Exp−1)×100%	
A''		31.562				
B''		1.5877			−0.5 {−0.8} [+5.4][e]	
C''		1.4867			−0.7 {−0.6} [+5.0][e]	
$\Delta''_J\times10^4$		1.165			+4.0 {−6.5} [−5.5][e]	
$\delta''_J\times10^6$		7.0				
$\overline{B}''$	1.5394	1.5371	1.5304	−0.7 {−0.8} [+5.1][f]	−0.6 {−0.7} [+5.2][f]	−0.7 {−0.7} [+5.2][f]
$\overline{D}''\times10^4$	1.260[g]	1.19	1.13	−0.9 {−11.} [−4.0][f]	+6.3 {−4.6} [+0.1][f]	−3.4 {−13.} [−11.][f]
A'		30.263				
B'		1.5824			−0.6 { +0.1}	
C'		1.4797			−0.7 { +0.4}	
$\Delta'_J\times10^4$		1.132			+1.9 {−107}	
$\delta'_J\times10^6$		6.9				
$\overline{B}'$	1.5332	1.5310	1.5248	−0.7 {+0.0}	−0.7 { +0.3}	−0.7 { +0.8}
$\overline{D}'\times10^4$	1.234	1.16	1.09	−1.0 {−99.}	+4.4 {−104}	−4.9 {−134}
$A''-A'$		1.299			+3.3 {+11.1}	

[a]Extracted from the calculated energies for J^e=0–16, $J^{e,f}$=1–12, and 2–10 levels in k=0, k=1 and k=2 groups, respectively. The energies in k=1 groups were fitted to eigenvalues of Watson's Hamiltonian, Eq. (26), truncated to two centrifugal distortion terms, giving the constants A, B, C, Δ_J, and δ_J. The calculated uncertainties of the constants do not affect their figures shown here. The root mean square errors of the fits for v_r=0 and v_r=1 are 5.5×10^{-4} and 5.4×10^{-4} cm^{-1}, respectively. The constants $\overline{B}$ and $\overline{D}$ and the subband origins were obtained from fits of the energies in each subgroup k^p for p=e, f to second order polynomial in $J(J+1)$, see Table VII.

[b]The data obtained in Ref. 3 from separate fits to 30, 45, and 28 transition energies measured in the K_a=0–0, K_a=1–1, and K_a=2–2 subbands, respectively, are taken as reference here.

[c]Larger by 0.53 than the result obtained from the same PES in Ref. 8, mainly because of using the nuclear masses in the present calculations.

[d]The numbers in braces concern the calculations of Ref. 9. The parameters were extracted from the energies given in that paper using the fitting procedure described in footnote *a*. The obtained values A''=31.0893(9), B''=1.58346(5), and C''=1.48796(7) are close (as they should) to the values of the rotational matrix elements $\frac{1}{2}\langle A\rangle_{11}$=31.11, $\frac{1}{2}\langle B\rangle_{11}$=1.586, and $\frac{1}{2}\langle C\rangle_{11}$=1.492 cm^{-1}, respectively, listed in Table 5 of Ref. 9. The rotational constants obtained for the state [1 0 0] are: A'=29.6895(1), B'=1.59320(9), C'=1.49735(9).

[e]These deviations concern the constants deduced from the (8) energies calculated (for K_a=1) in Ref. 3 using the PES of Ref. 6. The deduced rotational constants: A''=31.1908(2), B''=1.68175(9), C''=1.57134(9).

[f]Concern the constants obtained in Ref. 3 from the energies calculated in that work using the PES of Ref. 6.

[g]Larger by 7% and therefore much closer to the experimental value than the result obtained from the same potential in Ref. 8; the most likely cause are too big rounding errors of x the energy values used in the fit of that work.

TABLE IV: Infrared spectrum of Li^+–H_2. The v_r=0→1 band. The calculated origins of K_a=0–0, 1–1, and 2–2 subbands (ν_0), rotational (A, B, C) and centrifugal distortion (Δ_J, δ_J) constants[a] in the initial and final vibrational states, and their deviations from experimental data[b]. A comparison with previous calculations. Except for the percentage deviations, the entries are in cm^{-1}.

				Cal − Exp		
	K_a=0	K_a=1	K_a=2	K_a=0	K_a=1	K_a=2
ν_0	4053.097[c]	4049.055(8)[d]	4037.718(2)	−0.263 {5.53}[f]	−0.285 {5.15}[f]	−0.321 {4.52}[f]
				(Cal/Exp−1)×100%		
A''		65.531(4)[e]				
B''		2.5483(1)			−0.6 { 0.7}[g] [4.6][h]	
C''		2.3981(1)			−0.6 { 1.4}[g] [4.5][h]	
$\Delta''_J\times10^4$		3.252(4)			2.2 {−20.8}[g] [−1.2][h]	
$\delta''_J\times10^5$		1.59(3)			−6.5 {−23.5}[g] [−32.9][h]	
$\overline{B}''$	2.4782	2.4724	2.4558(1)	−0.6 { 1.0}[g] [4.5][i]	−0.7 { 1.0}[g] [4.5][i]	− 0.8 { 0.8}[g] [4.4][i]
$\overline{D}''\times10^4$	3.296(2)	3.22[j]	3.17[j]	0.2 {−20.7}[g] [−0.6][i]	1.3 {−21.4}[g] [−0.3][i]	−22.7 {−39.0}[g] [−24.9][i]
$A'-A''$		− 4.050(4)			0.7 { 8.7}[f]	
B'		2.5360(1)			−0.7 { 2.1}[f]	
C'		2.3841(1)			−0.7 { 2.7}[f]	
$\Delta'_J\times10^4$		3.121(4)			2.0 {−46. }[f]	
$\delta'_J\times10^5$		1.57(3)			7.5	
$\overline{B}'$	2.4645	2.4595(12)	2.4445(1)	−0.7 { 2.5}[f]	−0.7 { 2.5}[f]	− 0.8 { 2.8}[f]
$\overline{D}'\times10^4$	3.178(6)	3.11(5)	3.05	−0.7 {−20.9}[f]	1.6 {−13.7}[f]	−10.3 {−17.9}[f]

[a]Obtained for each [v_r 0 0] state by least-squares fitting of 30 energies in k=1 group, for $J^{e,f}$=1–15, to eigenvalues of a truncated Watson's Hamiltonian, see Table III. The root mean square errors of the fits for v_r=0 and v_r=1 are 9.1×10^{-3} and 9.5×10^{-3} cm^{-1}, respectively. The constants $\overline{B}$ and $\overline{D}$ and the subband origins ν_0 were obtained as described in Tables VII and VIII.

[b]From Ref. 4; the data from separate fits to transition energies measured in each of the three subbands.

[c]Larger by 1.127 cm^{-1} and by the same amount closer to the experimental value than the result obtained from the same potential in Ref. 8. In ∼92% this is an effect of using the nuclear masses in the present work.

[d]In parentheses are the calculated uncertainties of the constants in their last figures shown.

[e]Larger than the values resulting from the PESs of Refs. 9 and 6. See footnotes *g* i *h*.

[f]Obtained from the positions of $R(J)$ and $P(J)$ lines for $J\leq5$ and the energy levels in the [0 0 0] state calculated in Refs. 10 and 9, respectively. A'=58.306(15), B'=2.607(4), C'=2.465(4).

[g]Deviations from experiment of the rotational constants extracted from the (20) energies which were calculated (for K_a=1) in Ref. 9. The obtained values A''=62.676(1), B''=2.5827(1), and C''=2.4459(1) agree well with the respective elements in Table 5 of that paper: 62.71, 2.589, and 2.455.

[h]These deviations concern the constants deduced from the (8) energies calculated (for K_a=1) in Ref. 4 using the PES of Ref. 6: A''=64.4759(1), B''=2.68137(4), C''=2.521136(4).

[i]Concern the constants resulting from the PES of Ref. 6 which were calculated in Ref. 4.

[j]Significantly different values of these constants, of 2.65 and 3.6×10^{-4} for K_a=1 and K_a=2, respectively, are presented as results from the same PES in Ref. 4. Evidently, they were not calculated de novo there but were extracted from the rotational enegies provided in Ref. 8 up to single decimal figure only.

TABLE V: Li^+–D_2. Comparison with experiment of quantities related to energy splitting of f- and e- parity J states in k=1 groups of [0 0 0] and [1 0 0] vibrational states.

				$(X/X^{\rm Exp}-1)\times 100\%$[a]		
J	Δ_1''[b]	Δ_1'[b]	$\overline{\Delta}$[b]	$X=\Delta_1''$	$X=\Delta_1'$	$X=\overline{\Delta}$
1	0.403[c,e]	0.411[c]	0.102	0.7 {−5.0} [10.0][d]	0.2 {−7.3}	4.1 {−8.2}
2	0.906[e]	0.923	0.305	−1.8 {−6.8} [7.5]	0.8 {−5.0}	−0.7 {−5.5}
3	1.608[e]	1.637	0.609	−1.1 {−6.5} [8.3]	−0.8 {−6.7}	−0.7 {−6.6}

[a] $X^{\rm Exp}$ taken from Table III of Ref. 3. The values $\Delta_1''(3)$=1.626 and $\Delta_1'(3)$=1.650 deduced from the provided transition wavenumbers.

[b] $\Delta_1^\epsilon(J)=\Delta^\epsilon(J)+\Delta^\epsilon(J+1)$ for $\epsilon=\prime, \prime\prime$, and $\overline{\Delta}(J)=[\Delta'(J)+\Delta''(J)]/2$, where $\Delta''(J)$ and $\Delta'(J)$ denote the splitting $E(f)-E(e)$ of k=1 J levels in the v_r=0 and v_r=1 states, respectively. All Δ's are given in cm^{-1}. The directly measured quantities are: $\Delta R(J)=\Delta'(J+1)-\Delta''(J)$ and $\Delta P(J)=-\Delta'(J-1)+\Delta''(J)$, shown in left panel of Fig. 5, and $\Delta Q(J)=2\overline{\Delta}(J)$ — in right panel of this figure.

[c] The values of $\Delta_1^\epsilon(J)$ for $\epsilon=\prime, \prime\prime$ fit well to the expression $[B^\epsilon-C^\epsilon-4\delta_J^\epsilon(J^2+2J+2)](J+1)^2$ with the parameters B^ϵ, C^ϵ and δ_J^ϵ from Table III. An analysis of the quantities $\Delta_1^\epsilon(J)$ based on fits to complete Hamiltonian (26) is given in Fig. C1.

[d] The deviations in braces concern the results of Ref. 9, in brackets — the results calculated in Ref. 3 from the PES of Ref. 6.

[e] Available from Ref. 8 up to first decimal figure.

TABLE VI: Same as in Table V for Li^+–H_2.

				$(X/X^{\rm Exp}-1)\times 100\%$[a]		
J	Δ_1''[b]	Δ_1'[b]	$\overline{\Delta}$[b]	$X=\Delta_1''$	$X=\Delta_1'$	$X=\overline{\Delta}$
1	0.599[c]	0.607[c]	0.151	−2.0 {−10.0} [4.7][d]	−3.2 {−13.9}	−1.9 {−12.3}
2	1.346[e]	1.365	0.452	−1.0 { −9.6} [5.7]	0.6 { −9.7}	−2.8 {−11.8}
3	2.386[e]	2.399	0.903	0.2 { −8.4} [7.0]	−0.8 {−10.3}	1.1 { −8.5}
4	3.713[e]	3.731	1.489	−1.2 { −9.8}	−1.0 { −9.9}	−1.2 { −9.9}
5	5.321	5.367	2.233	−1.2 { −9.7}	−1.1	−1.0 { −9.8}

[a] $X^{\rm Exp}$ taken from Table III of Ref. 4. The value $\overline{\Delta}(5)$=2.256 cm^{-1} deduced from the data for J=4 using the relation $\Delta_1'(J)+\Delta_1''(J)=2[\overline{\Delta}(J)+\overline{\Delta}(J+1)]$ and the values $\Delta_1''(5)$=5.385 and $\Delta_1'(5)$=5.428 cm^{-1} obtained as $2\overline{\Delta}(5)+\Delta P(6)$ and $2\overline{\Delta}(5)+\Delta R(5)$, respectively.

[b,c] See the respective footnotes in Table V. The parameters for the analytical representation of the functions $\Delta_1^\epsilon(J)$ for $\epsilon=\prime, \prime\prime$ should be taken from Table IV.

[d] The deviations in braces concern the results of Refs. 9 and 10, in brackets — the results calculated in Ref. 4 from the PES of Ref. 6.

[e] The numbers available from Ref. 8 for these quantities, 1.3, 2.4 and 3.8 for J=2, 3, and 4, respectively, appear only slightly less consistent with experiment than the present numbers.

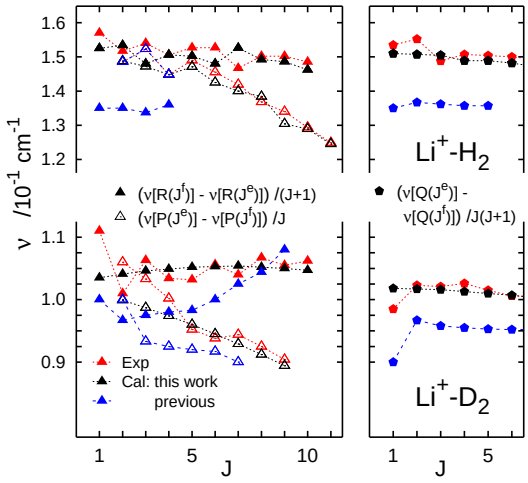

Fig. 5. The v_r=0→1 bands of the absorption spectra of the Li^+–$H_2(D_2)$ complexes; splitting of lines in the K_a=1–1 subbands due to transitions from the initial f- and e-parity states. Plotted are the frequency shifts $\nu[R(J^f)]-\nu[R(J^e)]:=\Delta R(J)$, $\nu[P(J^e)]-\nu[P(J^f)]:=\Delta P(J)$ and $\nu[Q(J^e)]-\nu[Q(J^f)]:=\Delta Q(J)$ divided by J+1, J, and $J(J+1)$, respectively. The values calculated in this work and in Refs. 9–10 are confronted with the values measured in Refs. 3–4.

Rotational structures in $[\mathbf{v_r}\,\mathbf{v}_\theta\,\mathbf{v_R}]$ states with $\mathbf{v}_\mathrm{m}$=0−2 for m=$\mathbf{r},\theta,\mathbf{R}$.

To visualize the structures, sets of lowest rotational levels in the states were paramerized using two approaches, called below parametrization *P1* and *P2*, respectively.

Parametrization *P1* consists in fitting separately levels of parity p=e and p=f from each group k to second order polynomial in $J(J+1)$. The resulting parameters X^{k^p}=($E_\mathrm{o}^{k^p}$, B^{k^p}, and D^{k^p}) describe the k^p subgroup origin, the subgroup rotational and centrifugal distortion constants, respectively. The parameters X^{k^p} for at least three (k=0, $1^{e,f}$) subgroups of nine vibrational states, all but one with $\sum_\mathrm{m} v_\mathrm{m}\leq 2$, are listed in Tables VII and VIII.

Parametrization *P2* consists in exploitation of Watson's Hamiltonian, Eq. (26), which can represent sets of J levels from several k groups of a given vibrational state. Fits yielding all five centrifugal distortion parameters of this Hamiltonian with reasonable uncertainties appeared possible only for k=0−2 groups of levels in four vibrational states of the Li^+–D_2 complex; see Table CVI and Fig. C1. Therefore, resorting to truncated versions ${}_{(i)}H$, including only the first $2\leq i<5$ quartic terms listed in the second line of Eq. 26, was necessary. Fits to eigenvalues of Hamiltonians ${}_{(i)}H$ with i=2, 3, and 4 can represent levels in k=1, in k=0−1, and in k=0−2 groups, respectively, in terms of 3+i parameters ${}_{(i)}X$=${}_{(i)}A$, ${}_{(i)}B$, ${}_{(i)}C$ ${}_{(i)}\Delta_J$, ... The asymmetric top rotational constants obtained from the fits to the differently truncated Watson's Hamiltonian account effectively for different contributions of terms rejected. Namely, ${}_{(3)}A\approx A-\Delta_K$, ${}_{(3)}B\approx B-2\delta_K$, ${}_{(3)}C\approx C+2\delta_K$, ${}_{(2)}X\approx{}_{(3)}X-\Delta_{JK}$ for $X=A,B,C$, and ${}_{(4)}X\approx{}_{(3)}X$ for $X=B,C$, but ${}_{(4)}A\approx A$.

The two parametrizations are obviously not strictly equivalent but approximate relations between all the parameters ${}_{(i)}X$ for i=2−4 and the parameters X^{k^p} for k=0−2 can be established (see Table CVII). For i=2, they are: ${}_{(2)}A\approx\sum_p \frac{1}{2}(E_\mathrm{o}^{1^p}+B^{1^p})-E_\mathrm{o}^0$, ${}_{(2)}B\approx\frac{1}{2}(3B^{1^f}-B^{1^e})$, ${}_{(2)}C\approx\frac{1}{2}(3B^{1^e}-B^{1^f})$, ${}_{(2)}\Delta_J\approx\frac{1}{2}(D^{1^f}+D^{1^e})$, and ${}_{(2)}\delta_J\approx\frac{1}{2}(D^{1^f}-D^{1^e})$. Accuracy of these relations can be checked on the parameters of states [0 0 0] and [1 0 0] using the ${}_{(2)}X$s listed in Tables III and IV and the values of X^{k^p} from Tables VII and VIII. Deviations smaller than 0.1% occur between the approximate and 'exact' (fitted) values of the rotational constants. The

same consistency is observed in Tables IX and CVIII between the rotational constants obtained from fits to Hamiltonians ${}_{(3)}H$ and ${}_{(4)}H$ and their approximations obtained from the parameters X^{kp}.

${}_{(3)}H$ is the least truncated version of Watson's Hamiltonian which could be exploited for parametrization of rotational structures in a number of vibrational states of both complexes, Li^+–H_2 and Li^+–D_2. Thus, the values of ${}_{(3)}A$, ${}_{(3)}B$, and ${}_{(3)}C$ are the most appropriate data available on which the dependence of the rotational constants on the vibrational quantum numbers and effects of isotopic substitution on this dependence can be demonstrated. This demonstration is given in Table IX and Fig. 6.

The most striking effects displayed in Table IX are associated with the excitation of Li^+–H_2 from [0 0 0] to [0 1 0] state. The parameter ${}_{(3)}A$ increases by about 45 %. Both parameters ${}_{(3)}B$ and ${}_{(3)}C$ decrease by much smaller amounts but the small difference between them increases enourmously, by over 75 %. Though above two times smaller, the effects of v_θ=0→1 excitation in the Li^+–D_2 complex are also clearly larger than the effects of v_R=0→1 or v_r=0→1 excitation.

The question naturally arises about the adequacy of the semirigid asymmetric top model for application to the present complexes in the higher excited vibrational states mentioned in the title of this subsection. If the model is unreservedly applicable to these states, the rotational constants A, B, and C should show a linear dependence on the three quantum numbers v_r, v_θ, and v_R (cf. Ref. 44). The linearity is tested in Fig. 6 by comparing the values of ${}_{(3)}X$ (=A, B, C) in states states with $\sum_{\rm m} v_{\rm m}$=2, 3 to the values ${}_{(3)}\widehat{X}$ (=$\widehat{A}, \widehat{B}, \widehat{C}$) extrapolated from the constants in the four states with $\sum_{\rm m} v_{\rm m}\leq 1$,

$$\widehat{X}([v_r\, v_\theta\, v_R]) = X([0\,0\,0])\,\big(1-\sum_{\rm m} v_{\rm m}\big) + \sum_{\rm m} X([\delta_{{\rm m},r}\ \delta_{{\rm m},\theta}\ \delta_{{\rm m},R}])\, v_{\rm m}\,. \qquad (27)$$

As expected, the dependence on the number v_θ is superlinear. This is documented in the figure on the parameters for state [0 2 0] of Li^+–H_2: the relative deviations $({}_{(3)}X/{}_{(3)}\widehat{X}-1)\times 100\%$ are as large as 45 and 83 % for X=A and X=B−C, respectively. Thus, from physical point of view the semirigid top model appears inappropriate for this complex when excited in the bending mode above v_θ=1. Actually, even formal application of the model to v_θ>1 states of both complexes is rarely possible because of the more frequent and stronger perturbations of J levels that occur in the higher and more congested parts of the spectra, cf. Figs. 2–3.

Fig. 7 shows the K=1 doubling $\Delta([v_r\, v_\theta\, v_R], J)$ in several vibrational states of the complexes from the range considered here. In the states amenable to the parametrizations *P2* and *P1*, the J dependence of the doubling is well represented by the polynomial

$$\Delta([v_r\, v_\theta\, v_R], J) = a([\ldots])J(J{+}1) - b([\ldots])[J(J{+}1)]^2$$

with the parameters a and b being related to the parameters ${}_{(i)}X$ and X as $a\approx\frac{1}{2}({}_{(i)}B-{}_{(i)}C)\approx\frac{1}{2}(B-C)-2\delta_K$ and $b\approx 2\delta_J$. The overall size of the doubling is determined by the parameter a which, in turn, is determined mostly by the asymmetry B−C of the top describing given complex in a given state $[v_r\, v_\theta\, v_R]$. The contribution of the distortion parameter δ_K may be quite substantial, however, as indicated by the distances between the corresponding violet and blue symbols in Fig. 6c. Obviously, the parameter a changes with the vibrational quantum numbers the same as shown in Fig. 6c for ${}_{(3)}B-{}_{(3)}C$. It increases slightly and decreases visibly with growing v_r and v_R, respectively, and grows rapidly with v_θ. The parameter b, above three order magnitude smaller than a, shows a reverse dependence on the numbers v_r and v_R, i.e. a slight decrease and a visible increase, respectively, and even more rapid growth with the number v_θ; see Table IX and Fig. C2.

TABLE VII: Li^+–D_2. Rotational energy levels in $k^{p\{=e,f\}}$ subgroups of several vibrational states $[v_r\, v_\theta\, v_R]$ represented the polynomials $E(k^p;J)=E_o^{k^p}+B^{k^p}[J]-D^{k^p}[J]^2$ in $[J]=J(J+1)$ [a]. The energies are shown in cm^{-1} relative to the position of the ground state of the complex, at 1783.613 cm^{-1} below the dissociation threshold $D_2(v=0\, j=0)$ + Li^+.

k^p	$[v_r v_\theta v_R]$	$E_o^{k^p}$	B^{k^p}	D^{k^p} $\times 10^4$	σ $\times 10^3$	$N_{\rm fit}$	$[v_r v_\theta v_R]$	$E_o^{k^p}$	B^{k^p}	D^{k^p} $\times 10^4$	σ $\times 10^3$	$N_{\rm fit}$
0	[0 0 0][b]	0.000	1.5394	1.260	0.4	17	[1 0 0][b]	2915.445	1.5332	1.235	0.8	17
1^e		30.025	1.5119	1.11*7*	0.4	12		2944.180	1.5054	1.08*8*	0.5	12
1^f		30.025	1.5624	1.25*7*	0.4	12		2944.180	1.5567	1.227	0.2	12
2^e		119.700	1.5304	1.09*5*	0.4	10		3030.039	1.5248	1.05*9*	0.4	10
2^f		119.700	1.5304	1.16*2*	0.2	10		3030.039	1.5248	1.134	0.2	10
3^e		268.00*9*	1.5196	1.15*3*	0.5	10		3172.12*6*	1.514*6*	1.11*4*	3.5	10
3^f		268.010	1.5196	1.15*1*	0.4	10		3172.12*4*	1.514*7*	1.12*1*	3.3	10
4^e		473.59*8*	1.505*5*	1.12*7*	0.9	8		3369.16*2*	1.502*4*	1.11*7*	2.2	10
4^f		473.59*6*	1.5055	1.13*0*	1.4	10		3369.16*3*	1.502*4*	1.11*5*	2.1	10
0	[0 0 1]	333.14*1*	1.4373	1.32*3*	1.9	17	[1 0 1]	3251.34*4*	1.4344	1.28*7*	1.2	17
1^e		363.725	1.4115	1.17*5*	0.6	12		3280.595	1.4083	1.13*9*	0.4	12
1^f		363.725	1.4589	1.32*8*	0.6	12		3280.595	1.4566	1.28*8*	0.5	12
2^e		454.787	1.4291	1.217	0.1	10		3367.77*7*	1.426*1*	1.16*9*	1.8	10
2^f		454.788	1.4291	1.260	0.1	10		3367.77*7*	1.426*0*	1.2*21*	2.1	10
0	[0 1 0]	451.291	1.4781	1.334	0.4	17	[1 1 0]	3371.073	1.4694	1.297	0.6	17
1^e		488.31*9*	1.4407	1.12*7*	0.9	12		3406.03*4*	1.4331	1.10*4*	1.0	12
1^f		488.318	1.508*1*	1.31*7*	0.3	12		3406.03*5*	1.4998	1.28*0*	0.9	12
2^e		596.73*0*	1.463*6*	1.3*69*	1.1	7		3508.8*68*	1.455*7*	3.*120*[c]	4.8	7
2^f		596.73*0*	1.463*6*	1.3*92*	1.0	7		3508.8*69*	1.455*6*	3.*126*[c]	4.2	7
0	[0 0 2]	629.33*8*	1.3318	1.41*3*	4.2	17	[1 0 2]	3551.51*5*	1.3327	1.36*3*	3.1	17
1^e		660.561	1.3080	1.236	0.2	12		3581.350	1.3086	1.20*0*	0.5	12
1^f		660.561	1.3517	1.40*9*	0.7	12		3581.350	1.3533	1.36*4*	0.7	12
0							[2 0 0]	5710.216	1.5272	1.212	1.0	17
1^e								5737.74*0*	1.4992	1.06*6*	0.7	12
1^f								5737.741	1.5514	1.19*9*	0.4	12
2^e								5820.01*5*	1.5194	1.01*8*	0.7	10
2^f								5820.01*5*	1.519*4*	1.1*06*	1.5	6

[a]The coefficients of the polynomial were determined by least-squares fitting to $N_{\rm fit}$ lowest J levels obtained from the 3D calculations. Italic figures of the coefficients are uncertain according to the calculated uncertainties (not shown). Shown are the root mean square deviations σ between the fitted and calculated values.

[b]The parameters for k=0−2 are listed in Table III as $\overline{X}(k)=\frac{1}{2-\delta_{k,0}}\sum_p X^{k^p}$ for $X=B,D$. The origin ν_0 of $K_a=k$ subband of the v_r=0→1 band is obtained as $E_o(k;[1\,0\,0])-E_o(k;[0\,0\,0])$.

[c]Perturbed by interactions with levels from $k^p=3^p$ subgroups of state [1 0 1].

TABLE VIII: Same as in Table VII for Li^+–H_2 [a].

k^p	$[v_r v_\theta v_R]$	$E_o^{k^p}$	B^{k^p}	D^{k^p} $\times 10^4$	σ [b] $\times 10^3$	$[v_r v_\theta v_R]$	$E_o^{k^p}$	B^{k^p}	D^{k^p} $\times 10^4$	σ [b] $\times 10^3$
0	[0 0 0]	0.000[c]	2.4782	3.30	0.3	[1 0 0]	4053.097	2.4645	3.18	1.2
1^e		63.070	2.4349	3.06	0.7		4112.125	2.4218	2.98	4.7
1^f		63.070	2.5100	3.38	0.7		4112.124	2.4973	3.24	9.5
2^e		249.032	2.4558	3.18	1.6		4286.751	2.4445	3.05	1.4
2^f		249.033	2.4557	3.16	1.2		4286.752	2.4444	3.05	1.0
3^e		552.522	2.4294	3.17	3.3		4572.374	2.4205	3.04	2.5
3^f		552.525	2.4292	3.14	2.1		4572.374	2.4205	3.03	2.3
0	[0 0 1]	405.150	2.2625	3.56	0.6	[1 0 1]	4463.645	2.2593	3.40	0.5
1^e		470.791	2.2238	3.37	1.1		4524.924	2.2201	3.20	2.7
1^f		470.791	2.2930	3.72	1.1		4524.918	2.2911	3.62	6.5
2^e		660.968	2.2415	3.57	2.7		4703.548	2.2401	3.34	3.0
2^f		660.966	2.2417	3.39	3.2		4703.541	2.2405	3.27	2.1
0	[0 1 0]	594.332	2.3288	3.49	0.3	[1 1 0]	4658.524	2.3075	3.33	1.9
1^e		687.572	2.2554	3.11	1.8		4742.446	2.2412	3.00	5.3
1^f		687.575	2.3882	3.63	0.1		4742.455	2.3650	3.42	2.6
0	[0 0 2]	750.356	2.0359	3.92	0.8	[1 0 2]	4817.085	2.0451	3.70	0.9
1^e		818.962	2.0023	3.78	2.1		4880.973	2.0106	3.54	1.6
1^f		818.962	2.0647	4.15	2.2		4880.973	2.0743	3.90	1.7
0						[2 0 0]	7872.461	2.4520	3.10	5.6
1^e							7927.844	2.4069	2.44	6.8
1^f							7927.838	2.4854	3.08	4.9

[a]Of the parameters $E_o^{k^p}$, B^{k^p} and D^{k^p} for the states [0 0 0] and [1 0 0] formed are the subband origins ν_0 and the constants $\overline{B}$ and $\overline{D}$ listed in Table IV.

[b]$N_{\rm fit}$=10 energies were fitted in all cases shown except for the k=1^e and k=1^f subgroups of the state [2 0 0] where 7 and 9 energies, respectively, were used.

[c]Lies 1674.606 cm^{-1} below the threshold $H_2(v$=0 j=0) + Li^+.

TABLE IX: Rotational constants and selected centrifugal distortion parameters[a] characterizing J level structures of Li^+–aa (a=H,D) complexes in vibrational states $[v_r\, v_\theta\, v_R]$ with v_r+v_θ+v_R≤1. All entries in cm^{-1}.

	Li^+–D_2				Li^+–H_2			
	[0 0 0]	[1 0 0]	[0 0 1]	[0 1 0]	[0 0 0]	[1 0 0]	[0 0 1]	[0 1 0]
${}_{(3)}A^b$	31.563 ⟨+1⟩[c]	30.265 ⟨+3⟩	32.016 ⟨+5⟩	38.503 ⟨+3⟩	65.537 ⟨11⟩	61.487 ⟨ +5⟩	67.896 ⟨ +7⟩	95.573 ⟨−3⟩
${}_{(3)}B^b$	1.5900⟨−1⟩[c]	1.5846⟨−1⟩	1.4848⟨ 0⟩	1.5454⟨+1⟩	2.5538⟨−5⟩	2.5410⟨−10⟩	2.3330⟨−13⟩	2.4618⟨−2⟩
${}_{(3)}B-{}_{(3)}C^b$	0.1010⟨ 0⟩[c]	0.1027⟨−1⟩	0.0948⟨ 0⟩	0.1348⟨ 0⟩	0.1501⟨+1⟩	0.1519⟨ −9⟩	0.1385⟨ −1⟩	0.2646⟨ 10⟩
${}_{(3)}\delta_J\times 10^{5\,b}$	0.69 ⟨+1⟩[c]	0.69 ⟨ 0⟩	0.76 ⟨ 0⟩	0.97 ⟨−2⟩	1.59 ⟨+1⟩	1.57 ⟨−27⟩[d]	1.73 ⟨ +2⟩	2.32 ⟨28⟩
$\Delta_K\times 10$ [e]	0.332	0.283	0.593	2.15				
$\delta_K\times 10^2$ [e]	0.312	0.296	0.435	1.33				

[a]The parameters δ_K and δ_J contribute to K=1 doubling, see Fig. 7.

[b]From fits to the truncated Watson Hamiltonian ${}_{(3)}H$; details in Table CIX. Related to parameters of H, Eq. (26), as: ${}_{(3)}A\approx A-\Delta_K$, ${}_{(3)}B\approx B-2\delta_K$, ${}_{(3)}C\approx C+2\delta_K$, and ${}_{(3)}\delta\approx\delta_J$; see Tables CVI–CVII.

[c]In angle brackets: $({}_{(3)}\widetilde{X}-{}_{(3)}X)\times 10^\beta$ for X=$A, B, B-C$, and δ_J with β=3, 4, 4, and 7, respectively, where ${}_{(3)}\widetilde{X}$ denotes the respective value obtained from the parameters X^{k^p} listed in Tables VII and VIII: ${}_{(3)}\widetilde{A}=\frac{1}{2}(E_o^{1^e}+E_o^{1^f})-E_o^0+B^0$, ${}_{(3)}\widetilde{B}=B^0+B^{1^f}-B^{1^e}$, ${}_{(3)}\widetilde{B}-{}_{(3)}\widetilde{C}=2(B^{1^f}-B^{1^e})$, and ${}_{(3)}\widetilde{\delta}_J=\frac{1}{2}(D^{1^f}-D^{1^e})$.

[d]Large deviation due to inaccuracy of the paramaters D^{1^p} in this case; see Table VIII.

[e]Obtained from fits to H; details in Table CVI and Fig. C1.

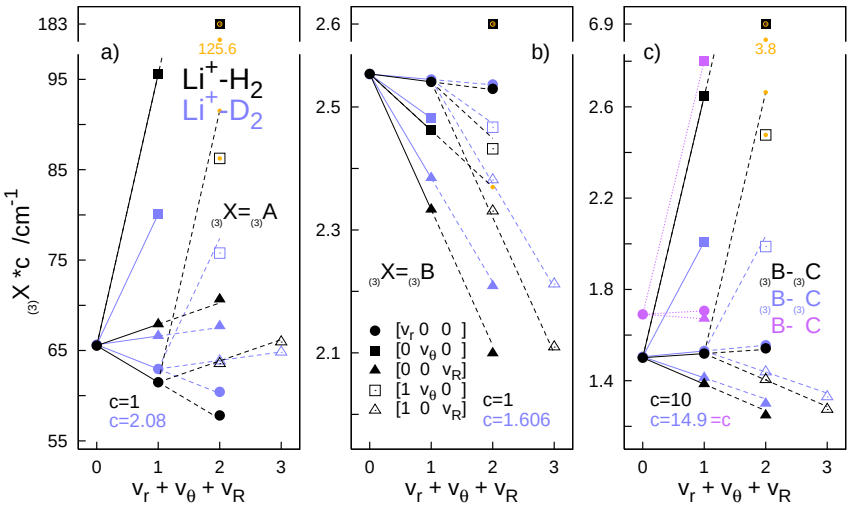

Fig. 6. Rotational parameters ${}_{(3)}A$, ${}_{(3)}B$, and ${}_{(3)}B-{}_{(3)}C$ of the semirigid asymmetric top characterizing the rotational level structures in nine vibrational states of the L^+–H_2 (D_2) complexes with combined excitation $v_r+v_\theta+v_R\leq 3$. The black and blue symbols represent the values of the parameters ${}_{(3)}X$ for $X=A, B, B-C$ obtained from fits to the truncated Watson's Hamiltonian ${}_{(3)}H$. See Tables BVI and CIX for details on the fits. The full lines show the changes of each of the parameters upon one-quantum excitation in one of the modes m=r, θ, R. The dashed line show the values ${}_{(3)}\widehat{X}$ for the higher excited states, with $\sum_{\rm m} v_{\rm m}=2, 3$, extrapolated linearly from the ${}_{(3)}X$'s for the four $\sum_{\rm m} v_{\rm m}\leq 1$ states, Eq. (27). The cases of largest departure from linearity, ${}_{(3)}X-{}_{(3)}\widehat{X}$, occurring in state [0 2 0] and [1 1 0] of Li^+–H_2, are marked with the yellow dots and labels. In panel c), the 'true' asymmetry $B-C$ of the tops describing the Li^+–D_2 complex in the $\sum_{\rm m} v_{\rm m}\leq 1$ states is shown for comparison with the values of ${}_{(3)}B-{}_{(3)}C$, see Table IX.

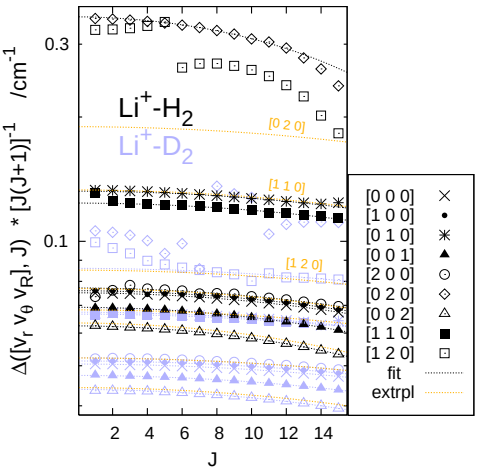

Fig. 7. K=1 doubling in several vibrational states of the Li^+–H_2 (D_2) complexes, $\Delta([v_r\, v_\theta\, v_R], J) := E([v_r\, v_\theta\, v_R]\, k=1, J^f) - E([v_r\, v_\theta\, v_R]\, k=1, J^e)$.
In most of the states shown, $\Delta(J)\approx a\, J(J+1) - b[J(J+1)]^2$, the polynomials plotted as the 'fit' lines, where $a\approx\frac{1}{2}({}_{(3)}B-{}_{(3)}C)\approx\frac{1}{2}(B-C)-2\delta_K$ and $b\approx 2\delta_J$ (Table IX, and Figs. 6c). The 'extrpl' lines are plotted for states with $\sum_{\rm m} v_{\rm m}>1$ using values of a and b extrapolated linearly from the values for states with $\sum_{\rm m} v_{\rm m}\leq 1$. Note the large separation between the 'extrpl' and 'fit' lines for state [0 2 0] of Li^+–H_2 — effect of superlinear growth of the parameters a and b with the number v_θ. See Fig. C2 for more details.

TABLE X: Widths (in cm^{-1}) of vibrationally predissociating states of the Li^+–$H_2(D_2)$ complexes used in the determination of the frequencies shown in Table II. Correlation with the redshifts. Comparison with the widths calculated in Ref. 7 from the PES of Ref. 6.

		$\Gamma([v_r\, v_\theta\, v_R]\, J{=}0)$					$\Gamma/(\Delta\nu)^2$ [a]
	v_r	$v_\theta{=}v_R{=}0$	$v_R{=}1$	$v_R{=}2$	$v_\theta{=}1$	$v_\theta{=}2$	$\times 10^6$
Li^+–H_2	1[c]	2.37 (−2)[b]	6.84 (−2)	1.12 (−1)	1.67 (−2)	1.59 (−2)	2.03
		[1.50 (−2)][d]	[2.19 (−2)][d]	[2.66 (−2)][d]			
	2	1.09 (−1)	2.90 (−1)	4.70 (−1)	1.08 (−1)	2.80 (−2)	2.37
		[4.34 (−2)][d]	[6.05 (−2)][d]	[7.44 (−2)][d]			
	3	3.82 (−1)	8.92 (−1)	1.40	2.70 (−1)	1.05 (−1)	3.94
Li^+–D_2	1[c]	8.29 (−3)	2.52 (−2)	4.55 (−2)	9.00 (−3)	5.86 (−3)	1.36
	2	3.24 (−2)	8.94 (−2)	1.56 (−1)	5.18 (−2)	2.25 (−2)	1.31
	3	8.54 (−2)	2.26 (−1)	3.89 (−1)	8.71 (−2)	8.64 (−2)	1.55

[a] Γ — the widths from third column , $\Delta\nu$ — the redshifts from Table II.

[b] The numbers in parentheses are powers of 10.

[c] The widths of the states with $v_r{=}1$ have been previously determined in Ref. 8. The numbers provided there (up to third decimal digit) agree almost perfectly with the numbers listed here.

[d] Extracted from the lifetimes listed in Table 2 of Ref. 7.

C. VIBRATIONAL PREDISSOCIATION

Total VP widths. The widths are generally very sensitive to properties of the used PES, to details of the entailed coupling between the r- and R-, θ-modes, in particular. Thus, in view of the differences in the mode's frequencies and anharmonicities exhibited in Tables II and BIII, a good consistency of the widths obtained from the present PES and the PES of Ref. 6 should rather not be expected. Actually, in the case of the lowest predissociating state $[1\,0\,0]\, J{=}0$ of the Li^+–H_2 complex the widths differ only by the factor of 1.6. However, the five other widths available from Ref. 7 depart more significantly from their present counterparts. As shown in Table X, they are smaller by factors ranging from 2.5 for state $[2\,0\,0]$ to 6 for $[2\,0\,2]$.

In the remainder of this subsection presented is a list of observations made on properties of the VP widths generated in this work, concretely, on dependencies of the widths on the vibrational and rotational quantum numbers of the predissociating states and on effects of the H→D substitution.

(c1). Dependence on v_r, approximately quadratic, is exhibited by the widths $\Gamma([v_r\,0\,0]\, J{=}0)$ of $Li^+{-}D_2$ listed in Table X. Combined with the ∼linear dependence of the redshifts $\Delta\nu$ of $0{\rightarrow}v_r$ transition frequencies, this gives the approximately constant ratios $\Gamma/(\Delta\nu)^2$ — the correlation observed experimentally in many van der Waals complexes and analyzed in Ref. 46. It should be added that in the present complexes the occurrence of the correlation is limited to the few lowest v_rs. In Li+–H_2, a significant departure occurs already for $v_r{=}3$, as demonstrated in the last column of Table X. However, in the small ranges of validity, $v_r^{\max}{=}2\,(3)$ for Li+–$H_2\,(D_2)$, the $\sim v_r^2$ scaling concerns not only the widths $\Gamma([v_r\,0\,0]\, J{=}0)$ but also the widths of vibrational states excited additionally in the R-mode, which can be noted in Table X and is clearly demonstrated in Fig. D14c, and also the widths of ro-vibrational states $[v_r\,0\,0]\,k\,J$, which is documented in Fig. D16c.

(c2). Dependence on v_R is demonstrated in Fig. 8 on the widths of the lowest rotational levels ($J{=}k$) in several groups k of states $[v_r{=}1\, v_\theta{=}0{-}1\, v_R]$. The functions $\Gamma(v_R; v_\theta\, k)$ are shown by the k-curves in separate panels panels a) and b) for $v_\theta{=}0$, and 1, respectively. Qualitatively describing, all curves have Gaussian-like shapes. Their maxima occur at $v_R{=}4\,(5)$, i.e. near the centres of the ranges of variation of this number among the states of the Li^+–$H_2\,(D_2)$ complexes below the $v{=}1\, j{=}v_\theta{+}k$ thresholds, $v_R^{\max}{=}10\,(12)$. In addition to the shift in the maxima position, the curves pertaining to Li^+–D_2 are considerably shifted

down relative to their Li^+–H_2 counterparts. In panel c), the v_R-dependence of the widths of levels from the groups v_θ=0 k=1−5 is shown in an implicit way; the plotted curves represent superposition of the functions $\Gamma(v_R; v_\theta\, k)$ with functions $v_R(|E_{kv_R}-\varepsilon_{v=1\, j=v_\theta+k}|^{\frac{1}{2}})$, nearly linear as shown in Fig. D15b. This way facilitates the comparison between the complexes. It appears that three curves pertaining to Li^+–D_2, for k=0, 1, 2, can be made nearly-coincident with their Li^+–H_2 counterparts by scaling them with the mass factor $(\frac{\mu_{\rm DD}}{\mu_{\rm HH}})^{\frac{1}{4}}\frac{\mu_{\rm Li^+-DD}}{\mu_{\rm Li^+-HH}}$ (deduced from the CM analysis presented in Fig. D14).

The non-monotic dependence of the widhts Γ on the number v_R, noted already in the pioneering work of Beswick and Jortner, Ref. 47. is certainly not explainable by a single factor. The fast increase in the low v_R range seems to originate from the 'initial condition' to the half-collision in the P-subspace, see Sec. IIA and *c3* below.

(c3). Dependence on v_θ in the range 0−2 (5) can be observed in the sets of widths of purely vibrational states of the Li^+–H_2 (D_2) complexes $[v_r$=1−3 v_θ v_R=0−$v_R^{\rm max}]$ J=0, which are listed in Tables IX and DI–II, and in the sets of widths of ro-vibrational states $[1\, v_\theta\, v_R$=0−$v_R^{\rm max}]\, k\, J$, which are shown in Figs. 8a–b and D15c (for J=k levels), and in Figs. 10a and 10c. The main observation is that the effect of excitation of the θ-mode on the widths is different than the effect of excitation of the R-mode (up to v_R=4, 5, at least). Namely, the widths tend to decrease upon the increase of v_θ. In Li^+–H_2(v=1), the decrease is substantial (by about 50%) already for v_θ=1. In Li^+–D_2, it begins at v_θ=2 and becomes quite sizeable for v_θ=4, 5. More precisely, the latter concerns the widths of J=0 levels in states [1 v_θ=4–5 0] which drop below the value for v_θ=0 by more than 100% as indicated by the arrows in Fig. 9c. Analogous tendency as to the effects of the intermolecular bending and stretching excitations on the VP widths has been previously observed in rare gas–halogen diatom van der Waals complexes[35,48,51]. The explanation suggested in Ref. 48 is confirmed here using the 3D-CM approach: the overall size of the term driving the coupled equations in the P-subspace, measured by the integral $\langle \mathbf{F}_Q\mathbf{H}_{QP}|\mathbf{H}_{PQ}\mathbf{F}_Q\rangle_R$, does indeed reflect the different impact of the excitation of the two modes.

(c4). Dependence on J *and* k of the widths of rotational levels in the vibrational state [1 0 0] is shown in Fig. 9. Widths of p=e and p=f parity levels are shown by different symbols. In most cases, the splitting between them appears very small. Therefore, only occasionally widths of both parity levels will be included in further presentation. The main fact to note is that

(i) the widths decrease with growing number J, much faster in Li^+–H_2 than in Li^+–D_2, and increase with the number k, also faster in the lighter complex. Inspection of the energies transferred to translational motion of the fragments, estimated with the use of the respective populations P_j, indicates that the momentum gap law[47,49] can be invoked to rationalize this behavior of the widths (see Fig. D16d).

Information on behavior of the rotational level widths in several other vibrational states is provided in Fig. 10. In panel a), the widths in k=0 groups of states $[v_r\, v_\theta\, v_R]$ with $\sum_{\rm m} v_{\rm m}\leq$3 of both complexes are plotted as functions of $J(J$+1). It is shown that $\ln\Gamma$ decreases approximately linearly with growing $J(J$+1), especially in states with v_θ=0; the slope of line for each vibrational state is determined by the respective rotational constant $B^{k=0}([\ ])$. This suggest that the widths $\Gamma([v_r\, 0\, v_R]\, k\, J)$ of both complexes should decline with approximately the same rate when expressed as function of the rotational energy $E([\ ]\, k\, J)-E([\ ]\, k\, J$=$k)$. Actually, it was found profitable (see Fig. D16b) to replace the rotational energy with the distance of the level $E([\ ]\, k\, J)$ from the threshold $\varepsilon_{v=v_r\, j=k}$. As functions of this 'binding energy', the widths of levels of Li^+−H_2 and of Li^+−D_2 appear related through a simple mass factor, the same for levels of at least four vibrational states. Namely, as demonstrated in panel b) of Fig. 10,

(ii) the widths $\Gamma([\ ]\, k\, J)$ in each of the four states [1–2 0 0] and [1 0 1–2] can be represented by the formula

$$\Gamma_{kJ}^{\rm Li^+-aa}=\frac{1}{s^{\rm a}}\, C\, \exp[-\beta(E_{kJ}^{\rm Li^+-aa}-\varepsilon_{v=v_r\, j=k}^{\rm aa})] \quad \text{with} \quad s^{\rm a}=\frac{\mu_{\rm aa}}{\mu_{\rm HH}}\,\frac{\mu_{\rm Li^+-aa}}{\mu_{\rm Li^+-HH}} \qquad \text{for a=H,D}\,.$$

The values of the parameters for state [1 0 0] — C=2.050×10^{-3} cm^{-1} and β=1.439×10^{-3} 1/cm^{-1}, and for state [2 0 0] — C=4×2.168×10^{-3} and β=1.320×10^{-3}, confirm the statement made in *(c1)* about the range of validity of v_r^2 scaling.

In Fig. 10c, the behavior of rotational level widths in states [1 v_θ 0] of Li^+–D_2 with v_θ growing up 5 is demonstrated. The most striking fact revealed is that

(iii) in states with the θ-mode excited to v_θ=4, 5 the widths behave completely differently than in the lower v_θ states, namely, they rapidly grow with the number J.

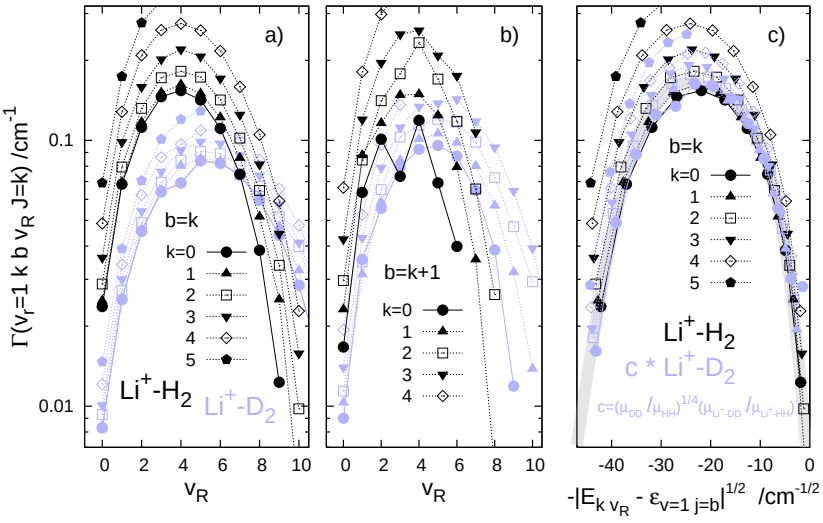

Fig. 8. Predissociation widths Γ of lowest rotational levels (J=k) in different groups k of various intermolecular vibration states [v_r=1 v_θ=b−k v_R] of the Li^+–H_2 (D_2) complexes. All widths shown are due to vibrational predissociation. Admixtures of rotational predissociation are either formally impossible or negligible (see Tables BI–BII, and CI–CII). In panels a) and b), the widths for v_θ=0, 1 and several values of k are shown as functions of the number v_R. In panel c) the functions $\Gamma(v_R; v_\theta\, k)$ for v_θ=0 and k=0–5, are re-plotted as functions of $-|E_{k\,v_R}-\varepsilon_{v=1\,j=b}|^{1/2}$, where $E_{k\,v_R}$ denotes the energy of state v_R from group k relative to the threshold v=0 j=0. Additionally, the widths of the Li^+–D_2 complex are multiplied by the mass factor c specified in the figure. In effect, the k=0, 1, 2-curves of the two complexes become close together what is marked with the gray strip.

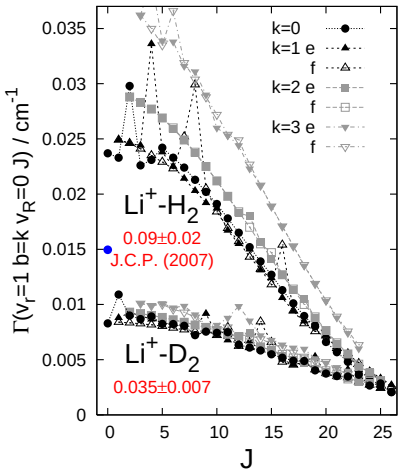

Fig. 9. Predissociation widths of rotational levels of the Li^+–H_2 and Li^+–D_2 complexes in their vibrational state [v_r v_θ v_R]=[1 0 0]. The upper bounds to these widths derived experimentally in Refs. 3 and 4 are quoted in the red labels. The blue symbol denotes the width of the lowest J=0 resonance of the Li^+–H_2 complex associated with the v=1 vibrational level of H_2 which was obtained in the calculations of Ref. 7.

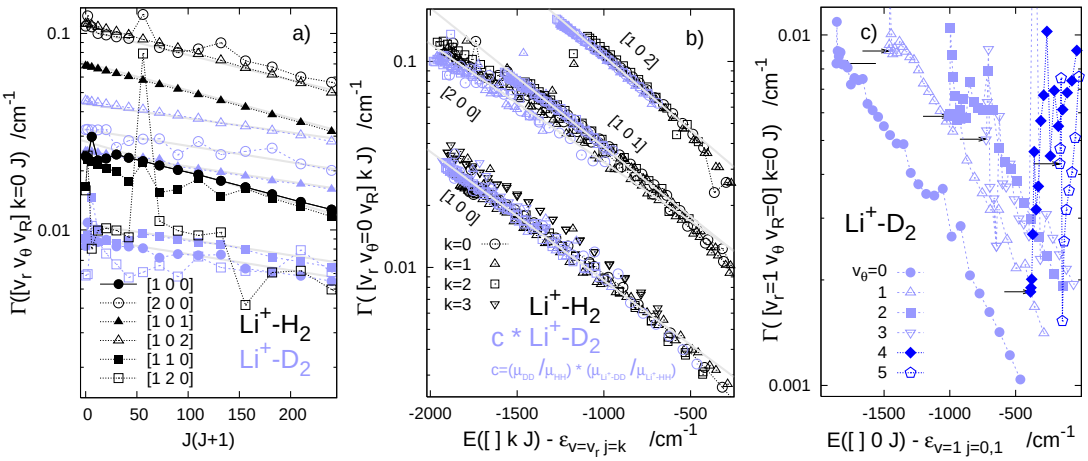

Fig. 10. Vibrational predissociation widths Γ of rotational $(k\,J)$ levels in several $[v_r{>}0\,v_\theta\,v_R]$ states. The widths are shown a) as functions of the number $J(J{+}1)$ and b) as functions of the energy position relative to the $\varepsilon_{v\,j}$ threshold with $v{=}v_r$ and $j{=}b{=}v_\theta{+}k$. The gray lines in panel a) show the declines of the functions $\exp[-\beta^{\rm a}B^{\rm a}J(J{+}1)]$ for the rotational constants $B^{\rm a}{=}B^{k=0}[v_r\,v_\theta\,v_R]$ taken from Table VII and VIII and $\beta^{\rm a}{=}1.24$ and $1.43{\times}10^{-3}$ for the complex with aa=D_2 and H_2, respectively. The gray lines in panel b) represent fits to the widths $\Gamma^{{\rm Li}^+-{\rm H}_2}([\ ]\,kJ)$ and $c{\times}\Gamma^{{\rm Li}^+-{\rm D}_2}$ in the four $[v_r\,0\,v_R]$ states shown. In panel c) are widths of states $[1\,v_\theta,0]\,k{=}0\,J$ of the Li^+–D_2 complex for v_θ growing from 0 to 5. For each v_θ, the dependence on the number J is shown implicitly through the energy $E([1\,v_\theta\,0]\,J){-}\varepsilon_{1\,j}$ with $j{=}0\,(1)$ for v_θ even (odd). The arrows indicate widths of $J{=}0$ levels in the different v_θ sets.

Partial widths. The widths Γ_{vj} for all $v\,j$ channels available in the predissociation of the complexes from their vibrational states $[v_r{=}1{-}3\,0\,0]\,J{=}0$ are shown in Fig. 11. Overall information is provided on the populations of the H_2 (D_2) product v-states ($P_v{=}\sum_j\Gamma_{vj}/\Gamma$) depending on the state v_r of the complex, and on the populations of the product j-states ($P_j(v){=}\Gamma_{vj}/\Gamma$) depending on the vibrational number change $\Delta v{:=}v_r{-}v$. The energies available ($E_{\rm avl}$) in the vibrational channels $Li^+ + {\rm aa}(v)$ which pertain to the six populations curves shown for each complex Li^+–aa in Fig. 11 and the energies disposed, according to these populations, into rotations of the diatomic fragment ($\overline{E_{\rm rot}}$) are listed in Table XI. The j-state populations in the important $\Delta v{=}1$ vibrational channel which follow the VP of the complexes from their vibrational states $[v_r{=}1{-}3\,v_\theta\,v_R]\,J{=}0$ for $v_\theta{=}0{-}3\,(5)$ and $v_R{=}0{-}9\,(12)$ and from a wide selection of ro-vibrational states $[v_r{=}1\,v_\theta\,v_R]\,k\,J\,p$, with $k{\in}[0,5]$ and $J{\in}[0,30]$, are presented in Tables DI–DII and in Figs. 12, D1b, and D13.

This material allows for several observations on how the product state populations depend on the initial states, on the degree of excitation in each of the vibrational modes and in the overall rotation. The observations are summarized in the following two sub-subsections.

(c5). Populations of product v-states are highly peaked at $v{=}v_r{-}1$ which is an expected effect, of course. The branching ratio for population of $\Delta v{>}1$ to $\Delta v{=}1$ channels in the decay of states $[v_r\,0\,0]\,J{=}0$ with $v_r{=}2$ and 3 is as small as 0.0089 (0.0043) and 0.020 (0.0093), respectively. The branching increases slightly if the initial state is excited additionally in the R-mode, e.g. the values 0.037 (0.017) are obtained for $[3\,0\,2]$ state.

(c6). Populations of product j-states, $P_j(v;[v_r\,v_\theta\,v_R]\,k\,J)$, display distinct properties depending on the value of Δv. Therefore it is convenient to categorize them as specified in the titles (italic) of the following two paragraphs.

In $v{=}v_r{-}1$ *channels*, the most prominent feature concerns correlation with the number v_θ. Namely,

(i) a strong $b{=}v_\theta{+}k\ \rightarrow\ j{=}b{+}2$ propensity occurs in the decay of $v_\theta{=}0$ states, e.g. $P_{j=b+2}(0;[1\,0\,0]\,k{=}b{=}J){\gtrsim}0.95$ for $b{=}0{-}5$. However, with increasing v_θ, the peak at $j{=}b{+}2$ lowers substantially and a tendency to populate the highest accessible j-state

develops. In the populations resulting from decay of states highly excited in the bending mode, like $[1\,4\text{–}5\,v_R]\,k\,J$ states of Li^+-D_2, the peak is at the highest available j-state and a lower maximum at $j<b+2$ appears. Detailed analysis within the 3D-CM approach (Figs. D3–D12) shows that both factors of the dissociation model underlying this approach have a role: (1) the 'initial condition' (the driving term $H_{PQ}\Psi_Q$) to the half-collision taking place in the P-subspace, and (2) the interactions within the P-subspace. The populations of j-states being the outcome of the half-collision can depend on the number b only through the function Ψ_Q. In turn, the propensity for the $j-b=2$ excitation of the diatom detaching from the Li^+ ion is established entirely in the P-subspace. Though seemed probable, the $L=2$ anisotropy of the coupling H_{QP} is not responsible for this excitation. The propensity vanishes, excitations to higher j-states become dominating, when the region of the strongest anisotropy of the potential V_{PP} in the P-subspace, $\theta\lesssim 45^\circ$ and $\gtrsim 135^\circ$, becomes accessible. Access to this region is controlled, however, by the driving term, by its extent in the θ-coordinate which obviously increases with the number v_θ of the state described by Ψ_Q.

As to correlations with the other quantum numbers of the predissociating states, the general observation is that they merely attenuate the $b=v_\theta+k \rightarrow j=b+2$ propensity. Namely, the comparisons of the populations: $P_j(v_r-1;[v_r\,0\,v_R]\,J=0)$ for $v_r=1$ versus $v_r=2,3$ (Fig. 11, Tables DI–II), $P_j(0;[1\,0\,v_R]\,k\,J=k)$ for $v_R=0$ versus $v_R>0$ (Fig. 12, Tables DI–II), and $P_j(0;[1\,0\text{–}1,v_R]\,k\,J)$ for $J=k$ versus $J>k$ (Figs. D1b, D13b,d) show that

(ii) the increase of each of the numbers v_r, v_R, and J of the predissociating state causes a broadening of the distributions P_j, mostly at the $j>b+2$ side. The anisotropy of interactions in the P-subspace, reflected by the magnitude of the torque function $\langle v=v_r-1|\frac{\partial}{\partial\theta}V_{\rm int}(r,R,\theta)|v\rangle_r$, increases with v_r. The broadening effect of the other two excitations on the distributions $P_j(0;[1\,0\text{–}1,v_R]\,k\,J)$ should be ascribed rather to the associated increase of the total energy available to the fragments, $E([1\,0\,v_R]\,k\,J)-\varepsilon_{v=0,j=0}$.

The populations from the states highly excited in the bending mode (Fig. D13), like the total widths of these states (Fig. 9c), behave differently upon the increase of J; the peaks at the highest accessible j-states gradually disappear.

In $v=v_r-2$ *and* v_r-3 *channels*, the distributions $P_j(v=v_r-\Delta v;[v_r\,0\,0]\,J=0)$ are significantly broader than in v_r-1 channels and the positions of maxima are shifted from $j=2$ to $j=6$ and $j=8\,(10)$, respectively (Fig. 11). This may be interpreted as a manifestation of sensitivity to the magnitude of the total energy available to the fragments in a given channel v. In the dissociation with $\Delta v=1,2$, and 3 transitions, the values of $E_{\rm avl}$ in $v=0$ channels increase like 1, 2.6 (3.5), and 4.1 (5.8), respectively (Table XI). Another factor which could influence the distributions P_j in the $\Delta v>1$ decays are the ro-vibrational couplings in the respective P-subspaces containing more than one v-state. Inspection of the ratios $\overline{E_{\rm rot}}/E_{\rm avl}$ in Table XI points to importance of this factor. While in the $\Delta v=1$ dissociation the ratios have nearly the same values for Li^+–D_2 and Li^+–D_2, they differ substantially between the two complexes dissociating with $\Delta v>1$.

TABLE XI: Dissociation of Li^+–aa (a=H,D) complexes from $[v_r{=}2{-}3\, v_\theta{=}0\, v_R{=}0]\, J{=}0$ states into Li^+ + aa($v{=}v_r{-}\Delta v$) channels for $\Delta v{=}1,2,3$. Total energy available ($E_{\rm avl}$) and average energy transferred to rotation of diatomic fragments ($\overline{E_{\rm rot}}$), both in $\rm cm^{-1}$.

		Li^+–H_2					Li^+–D_2				
Δv	v	$E_{\rm avl}{}^a$	$j_{\rm avl}$	$j_{\rm max}{}^b$	$\overline{E_{\rm rot}}{}^c$	$\frac{\overline{E_{\rm rot}}}{E_{\rm avl}}$	$E_{\rm avl}$	$j_{\rm avl}$	$j_{\rm max}$	$\overline{E_{\rm rot}}$	$\frac{\overline{E_{\rm rot}}}{E_{\rm avl}}$
1	0	2378.50	4	2	405.7	0.17	1131.84	4	2	186.4	0.16
	1	2039.31	4	2	510.6	0.25	932.43	4	2	254.6	0.27
	2	1723.57	4	2	531.6	0.31	744.57	4	2	240.2	0.32
2	0	6197.89	10	6	24.4	0.0039	3926.59	10	6	5.9	0.0015
	1	5637.85	10	6	37.9	0.0067	3612.76	10	6	9.8	0.0027
3	0	9796.42	12	8	1.4		6606.93	14	10	0.2	

[a] $E([v_r\,0\,0]\,J{=}0){-}\varepsilon_{v\,j=0}$ with $v_r{=}v{+}\Delta v$; see Tables DI–DII,
[b] Position of maximum in the distribution $P_j(v;[v_r\,0\,0]J{=}0)$, see Fig. 11.
[c] Obtained as $\sum_j P_j(v;[v_r\,0\,0]J{=}0){\times}(\varepsilon_{v\,j}{-}\varepsilon_{v\,0})$.

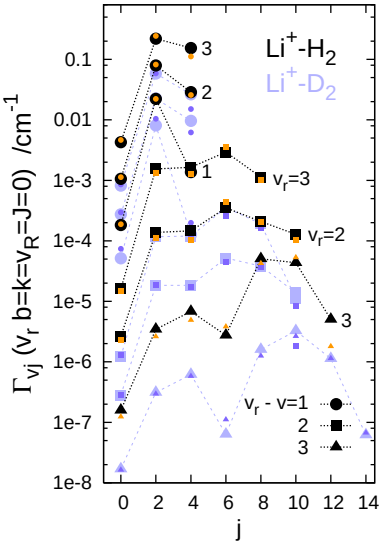

Fig. 11. Partial widths Γ_{vj} of $[v_r\,0\,0]\,J{=}0$ states of the complexes. The orange and dark-blue symbols represent results from the perturbative 3D-CM approach.

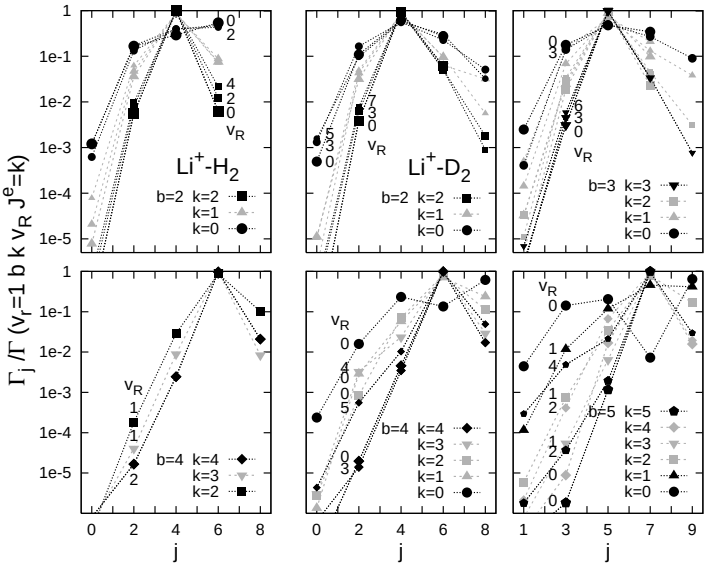

Fig. 12. Populations Γ_{0j}/Γ of $v{=}0\,j$ states of H_2 (D_2) in the vibrational predissociation of the $Li^+{-}H_2$ (D_2) complexes from states $[v_r{=}1\, v_\theta{=}b{-}k\, v_R]\, k\, J^e{=}k$ for $b{=}2,\ldots,5$, $k{=}0,\ldots,b$, and for several values of v_R.

D. ABSORPTION SPECTRUM

Absolute intensities.

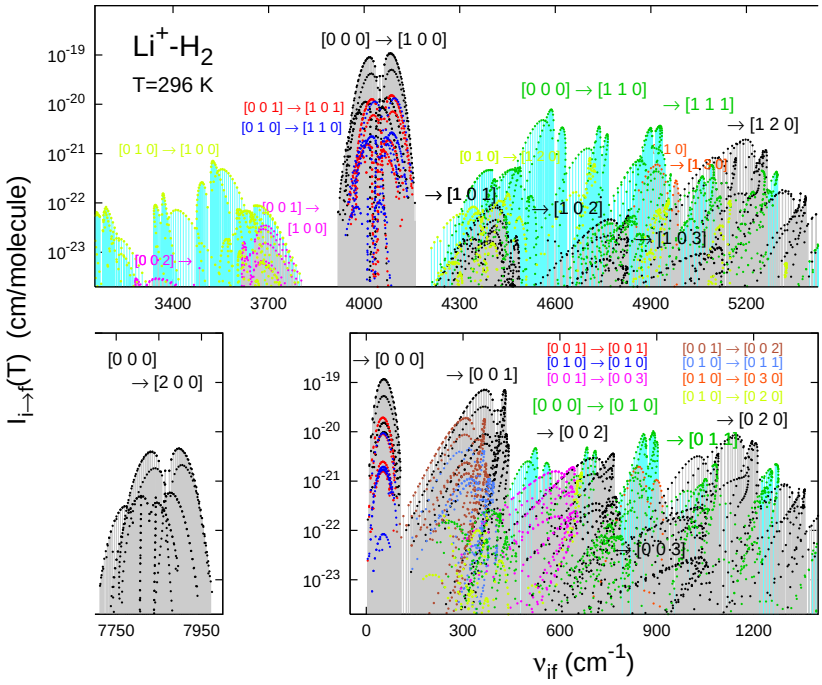

Fig. 13. Absolute intensities of lines in the infrared absorption spectrum of Li^+–H_2 at T=296 K. Lines due to i→f transitions of a-type (ΔK_a=0) and b-type (ΔK_a=±1) are distinguished by using grey and green, respectively, color for the sticks. Primary ([0 0 0]→[v'_r v'_θ v'_R]) and hot bands of the same type, a (Δv_θ even) or b, are distinguished by different colors of the circles on the top of the sticks. Altogether, 8620 lines are shown in the three panels of the figure. About 3170 of the lines belong to the b-type bands: [0 0 0]→[1 1 0], [0 0 0]→[1 1 1], [0 1 0]→[1 0 0], and [0 1 0]→[1 2 0] – in the near-infrared (NIR) and [0 0 0]→[0 1 0], [0 0 0]→[0 1 1], and [0 1 0]→[0 2 0] – in the far- and mid-infrared (FIR and MIR).

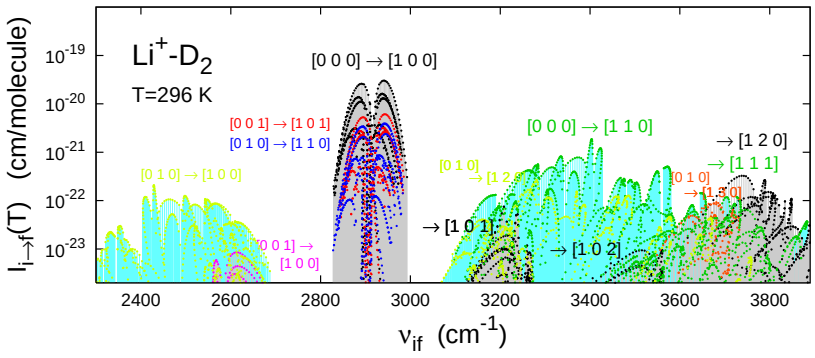

Fig. 14. Same as the upper panel of Fig. 13 for Li^+–D_2. 5665 lines are shown. Above halve of them (∼3000) belong to the four b-type bands. Intensities of above 6400 lines in fifteen other bands, mostly in the FIR, are presented in Fig. C3 (Ref. 55, Part C).

TABLE XII: Integrated vibrational band intensities ($I_{[\mathrm{v}'']\to[\mathrm{v}']}(T)$, in cm/molecule) in the infrared absorption spectra of Li^+–H_2 (D_2) at T=296 K.

	Li^+–H_2		Li^+–D_2	
$[\mathrm{v}'']\to[\mathrm{v}']$	$\nu_{[\mathrm{v}'']\to[\mathrm{v}']}$ [a]	$I_{[\mathrm{v}'']\to[\mathrm{v}']}$ [b]	$\nu_{[\mathrm{v}'']\to[\mathrm{v}']}$ [a]	$I_{[\mathrm{v}'']\to[\mathrm{v}']}$ [b]
[0 0 0]→[1 0 0]	4053.1	6.3 (−18)	2915.4	2.6 (−18)
→[0 1 0]	594.3	6.9 (−19)	451.3	2.1 (−19)
→[0 0 1]	405.1	4.4 (−18)	333.1	5.0 (−18)
[0 0 0]→[2 0 0]	7872.5	2.7 (−19)	5710.2	8.3 (−20)
→[0 2 0]	1068.2	4.3 (−19)	846.2	2.0 (−19)
→[0 0 2]	750.4	2.2 (−19)	629.3	2.3 (−19)
[0 0 0]→[1 1 0]	4658.5	4.6 (−19)	3371.1	1.7 (−19)
→[1 2 0]	5147.9	8.7 (−20)	3774.0	2.3 (−20)
→[1 1 1]	5010.5	4.5 (−20)	3675.4	1.1 (−20)
→[1 0 1]	4463.6	4.3 (−21)	3251.3	2.5 (−21)
[0 0 1]→[1 0 1]	4058.5	9.1 (−19)	2918.2	5.2 (−19)
[0 1 0]→[1 1 0]	4064.2	4.7 (−19)	2929.8	3.5 (−19)
→[1 0 0]	3458.8	2.9 (−20)	2464.1	2.1 (−20)
→[1 2 0]	4553.5	2.8 (−20)	3322.7	2.4 (−20)
[0 0 1]→[0 0 2]	345.2	1.2 (−18)	296.2	1.9 (−18)
[0 1 0]→[0 1 1]	346.3	1.8 (−19)	301.3	4.5 (−19)

[a]Band center taken as $[E([\mathrm{v}']\,J'=0)-E([\mathrm{v}'']\,J''=0)]/hc$ where $[\mathrm{v}]:=[v_r\,v_\theta\,v_R]$.

[b]Included into the sums of Eq. (9) are intensities of lines in the subbands $k''\to k'$ with $k''=0-3\,(4)$, $k'=k''$ for the bands with $\Delta v_\theta=0,2$, and $k'=k''\pm1$ for the bands with $\Delta v_\theta=\pm1$.

Linestrengths. Vibrational factors.

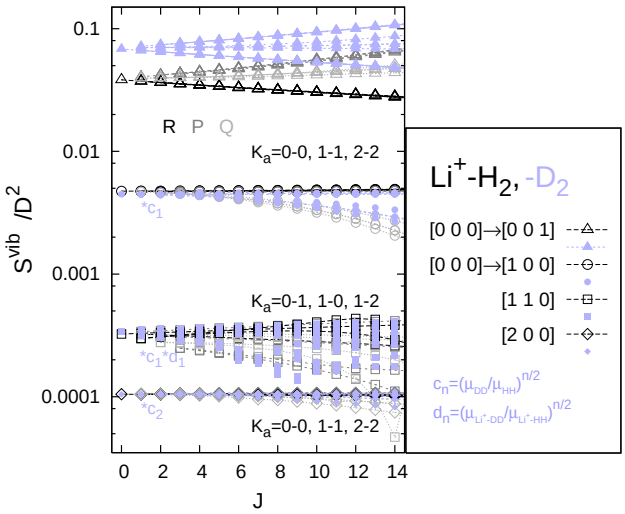

Fig. 15. Vibrational factors of line strengths in selected bands of the infrared spectra of Li^+–H_2 (D_2). The S^{vib}s of lines $R(J)$, $P(J)$, and $Q(J)$ in the subband $K_a=k\to k'$, with $k'=k$ in the three a-type bands ($v'_\theta=v_\theta$) and $k'=k\pm1$ in the b-type band, are results of dividing the strengths $S_{\mathrm{i}\to\mathrm{f}}$ of the lines (here i:=$([v_r\,v_\theta\,v_R]kJp)$ and f:=$([v'_r\,v'_\theta\,v'_R]k'J'p')$) by the rotational factors $S_{\mathrm{rot}}(Jk\to J'k')=(2J+1)|C(J1J',k\,k{-}k\,k)\,f^k_{k'-k}|^2$ with $J'=J+1, J-1$, and J, respectively, see Eqs. (21)–(24) and (C16)–(C18). The values of S^{vib} for lines of Li^+–D_2 in the bands with $v_r=0\to1,2$ excitations are enlarged in the figure by mass-factors related/analogous to that defined in Fig. 1b.

The S^{vib}s of $R(0)$ lines in the $v_R=0\to1$ and $v_r=0\to1$ bands of Li+–H_2 (D_2), $3.830\,(6.829)\times10^{-2}$ and $4.73\,(3.17)\times10^{-3}$ D^2, respectively, agree well with the vibrational strengths of $3.889\,(6.942)\times10^{-2}$ and $5.02\,(3.32)\times10^{-3}$ D^2 obtained in Ref. 5. A more extensive comparison in made in Table CXV.

Line heights in the NIR (bound→resonance transitions).

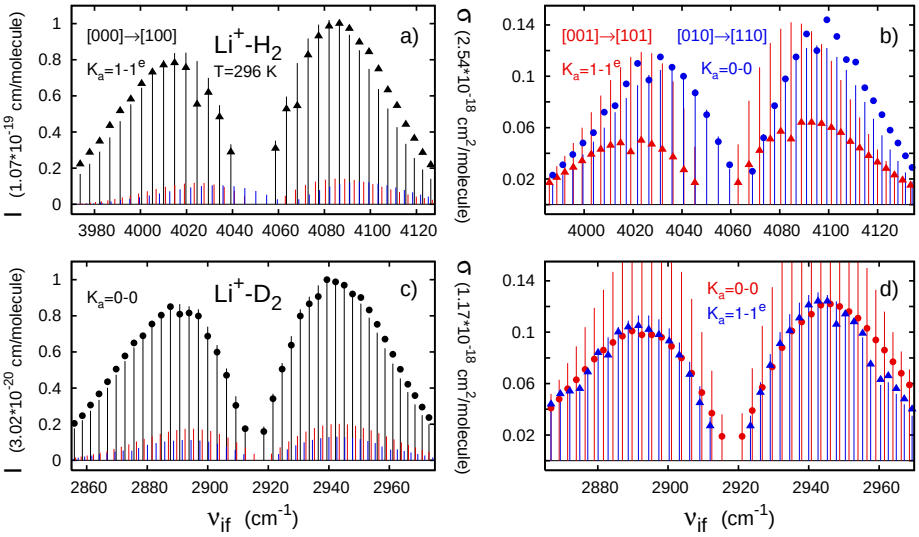

Fig. 16. A comparison of line intensities $I_{\mathrm{i}\to\mathrm{f}}(T)$ and line heights $\sigma_{\mathrm{i}\to\mathrm{f}}(\nu{=}\nu_{\mathrm{if}};T)$ in the absorption spectra of the Li^+–H_2 (D_2) complexes at T=296 K. The comparison is made on $R(J^e)$ and $P(J^e)$ lines in the most intense subband K_a of each of the three most intense vibrational bands in the NIR: the fundamental [0 0 0]→[1 0 0] and the hot [0 0 1]→[1 0 1] and [0 1 0]→[1 1 0] bands. The intensities are shown by the sticks and the line heights — by the symbols. The units of I and σ used in the upper (lower) panels are the values describing the highest lines in the spectra of Li^+–H_2 (D_2) which are the $R(7^e)$ lines at ν=4086.48 (2939.38) cm^{-1} in the K_a=1−1 (0−0) subbands of the fundamental bands.

Absorption cross-section.

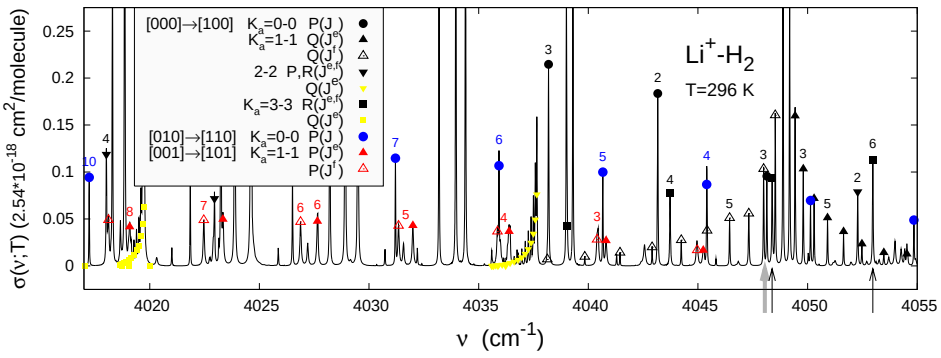

Fig. 17. A fragment of simulated near-infrared absorption spectrum of Li^+–H_2 at T=296 K. The shown frequency interval contains P lines of the two most intense hot bands which overlap with v_r=0→1 fundamental, see Figs. 13 and 15. The arrows on the ν axis indicate the lines of the fundamental band on which some information can be added to that provided by the experimental work, see Table XIII.

TABLE XIII: Infrared absorption spectrum of Li^+–H_2. Line positions (ν, in cm^{-1}), deviations from positions observed in Ref. 4 ($\Delta=\nu-\nu^{obs}$), vibrational factors of line strength (S^{vib}, in 10^{-3} D^2), and line intensities (I, in cm/molecule) at T=296 K in four subbands of v_r=0→1 band, $(b\,k{=}b\,v_R{=}0\,J\,p)\rightarrow(k\,k\,0\,J'\,p')$ for k=0–3. For each J in $k>0$ subbands, the entries in lower line concern $(Jp)\rightarrow(J\pm1\,p)$, $(J-p)$ transitions from initial $p=-1$ parity state. The asymmetric top labels of initial and final rotational levels, $J_{K_aK_c}$ and $J'_{K'_aK'_c}$, are: $K_a{=}K'_a{=}k$, $K_c{=}J{-}k{+}\frac{1-(-1)^k p}{2}$, $K'_c{=}K_c{+}\Delta K_c$ with $\Delta K_c{=}\pm1$ and $\Delta K_c{=}(-1)^k p$ for $J'{=}J\pm1$ and J, respectively [a].

	$R(J)$				$P(J)$				$Q(J)$			
J	ν	Δ	S^{vib} [b]	I [c]	ν	Δ	S^{vib} [b]	I [c]	ν	Δ	S^{vib} [b]	I [c]
						$k=0$						
0	4058.02	−0.31	4.73	1.16 (−20)								
1	4062.92	−0.34	4.74	2.28 (−20)	4048.14	[d]	4.74	1.13 (−20)				
2	4067.77	−0.38	4.74	3.26 (−20)	4043.17	−0.20	4.73	2.15 (−20)				
4	4077.31	−0.47	4.77	4.63 (−20)	4033.19	−0.15	4.72	3.63 (−20)				
5	4082.00	[e]	4.77	4.93 (−20)	4028.21	−0.14	4.74	4.03 (−20)				
6	4086.61	[e]	4.79	5.01 (−20)	4023.24	−0.12	4.74	4.19 (−20)				
7	4091.15	−0.61	4.79	4.85 (−20)	4018.30	−0.10	4.73	4.13 (−20)				
						$k=1$						
1	4058.70	−0.37	4.74	3.76 (−20)					4049.18	−0.31	4.68	3.71 (−20)
	4059.01	−0.37	4.72	3.75 (−20)					4048.88	−0.31	4.70	3.72 (−20)
2	4063.47	−0.41	4.73	6.39 (−20)	4039.30	−0.24	4.71	3.55 (−20)	4049.43	−0.33	4.62	1.94 (−20)
	4063.93	−0.41	4.72	6.35 (−20)	4039.00	−0.24	4.72	3.55 (−20)	4048.52	−0.30	4.66	1.95 (−20)
3	4068.21	−0.43	4.73	8.37 (−20)	4034.40	−0.22	4.71	5.88 (−20)	4049.80	−0.32	4.52	1.24 (−20)
	4068.80	−0.46	4.72	8.31 (−20)	4033.96	−0.20	4.72	5.87 (−20)	4048.00	−0.34[f]	4.58	1.25 (−20)
4	4072.86	−0.50	4.77	9.84 (−20)	4029.49	−0.19	4.70	7.49 (−20)	4050.30	−0.32	4.39	8.46 (−21)
	4073.62	−0.50	4.73	9.70 (−20)	4028.91	−0.19	4.71	7.47 (−20)	4047.32	−0.28	4.48	8.56 (−21)
6	4082.01	−0.58	4.79	1.09 (−19)	4019.71	−0.14	4.71	9.00 (−20)	4051.64		4.06	4.15 (−21)
	4083.05	−0.61	4.71	1.06 (−19)	4018.86	−0.13	4.73	8.91 (−20)	4045.42		4.28	4.30 (−21)
7	4086.48	−0.66[f]	4.81	1.07 (−19)	4014.84	−0.12	4.71	8.97 (−20)	4052.48		3.84	2.89 (−21)
	4087.70	−0.62	4.70	1.03 (−19)	4013.86	−0.10	4.72	8.82 (−20)	4044.24		4.13	3.04 (−21)
						$k=2$						
2	4052.28	−0.51	4.69	5.32 (−21)					4037.651	−0.38	4.60	1.04 (−20)
	4052.28	−0.51	4.69	5.32 (−21)					4037.651		4.60	1.04 (−20)
3	4057.06	−0.54	4.71	8.96 (−21)	4022.95	−0.29	4.67	4.90 (−21)	4037.585		4.52	6.66 (−21)
	4057.06	−0.54	4.71	8.96 (−21)	4022.95	−0.29	4.67	4.90 (−21)	4037.585		4.52	6.66 (−21)
						$k=3$						
3	4039.03	−0.69	4.69	3.56 (−21)					4019.746	−0.46	4.50	1.02 (−20)
	4039.03	−0.69	4.69	3.56 (−21)					4019.746		4.50	1.02 (−20)
4	4043.73	−0.71	4.70	5.95 (−21)	4000.39		4.65	3.18 (−21)	4019.678		4.40	7.01 (−20)
	4043.73	−0.72	4.70	5.95 (−21)	4000.39		4.65	3.18 (−21)	4019.681		4.40	7.01 (−20)
5	4048.38	[g]	4.71	7.46 (−21)	3995.55		4.65	5.17 (−21)	4019.595		4.28	4.94 (−20)
	4048.39	[g]	4.70	7.45 (−21)	3995.54		4.65	5.17 (−21)	4019.597		4.28	4.94 (−20)
6	4052.97	−0.83	4.73	8.29 (−21)	3990.72		4.66	6.32 (−21)	4019.509		4.12	3.48 (−20)
	4052.98	−0.83	4.73	8.29 (−21)	3990.72		4.66	6.32 (−21)	4019.502		4.12	3.49 (−20)

[a] Extended version of this Table, including all transitions measured and above 250 other transitions in the same band, is given in Supplementary Material [55].

[b] Obtained as $S^{vib}=S/S_{rot}$ with S_{rot} being here (cf. Fig. 15) the Hönl-London factor for $J\,k\rightarrow J'\,k$ symmetric top transitions[19], $S_{rot}(J\rightarrow J';k)=J{+}1{-}\frac{k^2}{J+1}$, $J-\frac{k^2}{J}$, and $\frac{2J+1}{J^2+J}k^2$ for $J'=J{+}1$, $J{-}1$, and J, respectively.

[c] Evaluated according to formulas (5)–(8). The value of $Z(296)$ is $687.65\times Z_{ref}$ where $Z_{ref}:=\exp(-E_0/k_B 296)$ is 3428.11. See Table BVII in Ref. 55.

[d] Line not measured. The cause appears to be the closeness to the $Q(3^f)$ line of the k=1 subband, as indicated by the gray arrow in Fig. 17.

[e] Not measured, probably because of strong overlapping with the $R(6^e)$ and $R(7^e)$ lines of the k=1 subband.

[f] Line observed as blended. This may be the cause of the slight local increase of $|\Delta|$.

[g] Missed in the measurements of Ref. 4; the ν values provided concern actually $R(6^{e,f})$ lines in the same (k=3) subband. The lines $R(5^{e,f})$ and $R(6^{e,f})$ are indicated by the black arrows in Fig. 17.

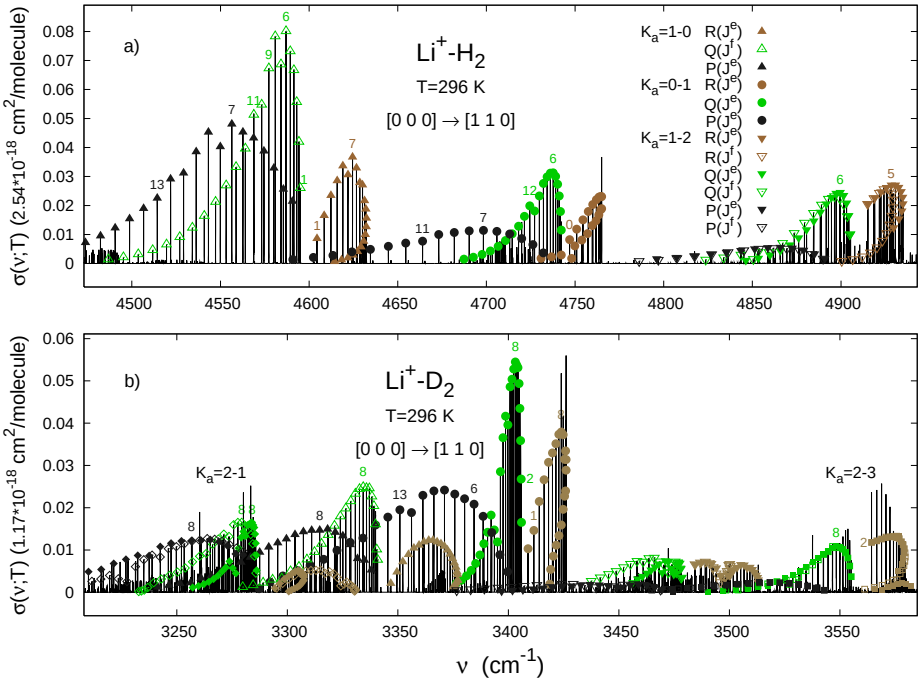

Fig. 18. The most intense combination bands in the near-infrared absorption spectra of the Li^+–H_2 (D_2) complexes.

[1] V. Dryza, B. L. J. Poad and E. J. Bieske, Phys. Chem. Phys., **14**, 14954 (2012).

[2] V. Dryza and E. J. Bieske, Intern. Rev. Phys. Chem. **32**, 559 (2013).

[3] C. D . Thompson, C. Emmeluth, B. L. J. Poad, G. H. Weddle, and E. J. Bieske, J. Chem. Phys. **125**, 044310 (2006).

[4] C. Emmeluth, B. L. J. Poad, C. D. Thompson, G. H. Weddle, and E. J. Bieske, J. Chem. Phys. **126**, 204309 (2007).

[5] V. P. Bulychev, K. M. Bulanin, and M. O. Bulanin, Opt. Spectrosc. **96**, 205 (2004).

[6] R. Martinazzo, G. F. Tandardini, E. Bodo, and F. A. Gianturco, J. Chem. Phys. **119**, 11241 (2003).

[7] C. Sanz, E. Bodo, and F. A. Gianturco, Chem. Phys. **314**, 135 (2005).

[8] W. P. Kraemer and V. Špirko, Chem. Phys. **330**, 190 (2006).

[9] A. J. Page and E. I. von Nagy-Felsobuki, J. Phys. Chem. **A 111**, 4478 (2007).

[10] A. J. Page and E. I. von Nagy-Felsobuki, Theor. Chem. Acc. **122**, 87 (2009).

[11] C. F. Curtiss and F. T. Adler, J. Chem. Phys. **20**, 249 (1952).

[12] J. Tennyson and B. T. Sutcliffe, J. Chem. Phys. **77**, 4061 (1982).

[13] L. C. Biedenharn and J. D. Louck, *Angular Momentum in Quantum Physics* (Addison-Wesley, 1981).

[14] R. G. Newton, *Scattering Theory of Waves and Particles*, Springer, New York, 1982.

[15] H. Feshbach, Ann. Phys. **5**, 357 (1958); **19**, 287 (1962).

[16] F. T. Smith, Phys. Rev. **118**, 349 (1960).

[17] J. M. Hutson, Advances in Molecular Vibrations and Collision Dynamics, Vol. 1A, p. 1–45 (1991).

[18] R. M. Stratt, N. C. Handy, and W. H. Miller, J. Chem. Phys. **71** 3311 (1979).

[19] R. N. Zare, *Angular Momentum* (John Wiley, 1988).
[20] R. C. Hilborn, Am. J. Phys. **50**, 982 (1981).
[21] M. Šimečková, D. Jacquemart, L. S. Rothman, R. R. Gamache, A. Goldman, JQSRT **98**, 130 (2006).
[22] A. M. Arthurs and A. Dalgarno, Proc. R. Soc. Lond. A**256**, 540 (1960).
[23] R.T. Pack, J. Chem. Phys. **60**, 2488 (1974).
[24] G. G. Balint-Kurti and M. Shapiro, Chem. Phys. **61**, 137 (1981).
[25] F. Mrugała, V. Špirko, and W. P. Kraemer, J. Chem. Phys. **118**, 10547 (2003).
[26] F. Mrugała and W. P. Kraemer, J. Chem. Phys. **122**, 224321 (2005).
[27] F. Mrugała and W. P. Kraemer, J. Chem. Phys. **138**, 104315 (2013).
[28] B. R. Johnson, J. Comput. Phys. **13**, 445 (1973).
[29] F. Mrugała, Int. Rev. Phys. Chem. **12**, 1 (1993).
[30] O. I. Tolstikhin, S. Watanabe, and M. Matsuzawa, J. Phys. **B29**, L389 (1996).
[31] F. D. Colavecchia, F. Mrugała, G. A. Parker, and R. T. Pack, J. Chem. Phys. **118**, 10387 (2003).
[32] M.-H Lee, C. W. Byun, N. N. Choi, and G. Tanner, Phys. Rev. A **81**, 043419 (2010).
[33] F. Mrugała and R. Moszynski, J. Chem. Phys. **109**, 10823 (1998).
[34] U. Fano, Phys. Rev. **124**, 1866 (1961); F. H. Mies, J. Chem. Phys. **51**, 787 (1969).
[35] N. Halberstadt, J. A. Beswick, and K. C. Janda, J. Chem. Phys. **87**, 3966 (1987).
[36] O. Roncero, J. A. Beswick, N. Halberstadt, P. Villareal, and G. Delgado-Barrio, J. Chem. Phys. **92**, 3348 (1990).
[37] A. A. Buchachenko, T. A. Grinev, J. Kłos, E. J. Bieske, M. M. Szczęśniak, and G. Chałasiński, J. Chem. Phys. **119**, 12931 (2003).
[38] B. L. J. Poad, V. Dryza, A. A. Buchachenko, J. Kłos, ans E. J. Bieske, J. Chem. Phys. **137**, 124312 (2012).
[39] K. K. Irikura, J. Phys. Ref. Data, **36**, 389 (2007). The value of ZPE(D_2) was taken from this paper to obtain $D_0(Li^+{-}D_2)$=1773.9 from the values of D_e and ZPE($Li^+{-}D_2$) provided in Ref. 9.
[40] The energy presented in Ref. 7 as the ZPE value of Li^+–H_2 above the well of the complex is actually relative to the asymptote of the PES. The estimations of the ZPE and of the D_0 of the Li^+–D_2 complex are based on the analysis of the vibrational frequencies presented in Table BIII (Ref. 55).
[41] Actually, f-parity states of the complexes Li^+–pH_2 (oD_2) are stable up to v=0 j=2 thresholds as they cannot decay to the j=0 channel. In the $[\varepsilon_{00}, \varepsilon_{02}]$ ranges, 195 (292) such states have been found.
[42] The bound→bound version of the formula for $S_{\mathrm{i}\to\mathrm{f}}$, obtained by removing the factor $\frac{\pi}{2}\Gamma$ from Eq. (19) and replacing ${}_{\mathrm{BF}}\mathbf{F}^{(+)J_{\mathrm{f}}p_{\mathrm{f}}}(E_{\mathrm{f}}^{\mathrm{res}})$ with ${}_{\mathrm{BF}}\mathbf{F}^{J_{\mathrm{f}}p_{\mathrm{f}}}(E_{\mathrm{f}}^{B})$ in Eqs. (20) and (21), is essentially identical to formula (16) of Ref. 43.
[43] S. Miller, J. Tennyson, B. T. Sutcliffe, Mol. Phys. **66**, 429 (1989).
[44] D. Papoušek and M. R.Aliev, *Molecular Vibrational-Rotational Spectra* (Elsevier, Amsterdam, 1982).
[45] J. K. G. Watson, J. Chem. Phys. **46**, 1935 (1967).
[46] R. J. Le Roy, M. R. Davies, and M. E. Lam, J. Phys. Chem. **95**, 2167 (1991).
[47] J. A. Beswick and J. Jortner, J. Chem. Phys. **68**, 2277 (1978).
[48] A. Garcia-Vela, J. Phys. Chem. A **118**, 6395 (2014).
[49] G. E. Ewing, J. Chem. Chem. **71**, 3143 (1979).
[50] J. C. Drobits and M. I. Lester, J. Chem. Phys. **89**, 4716 (1988).
[51] R. L. Waterland, M. I. Lester, and N. Halberstadt, J. Chem. Phys. **92**, 4261 (1990).
[52] Th. A. Stephenson, J. Chem. Phys. **97**, 6262 (1992); M. Nejad-Sattari and Th. A. Stephenson, J. Chem. Phys. **106**, 5454 (1997).
[53] J. P. Darr, R. A. Loomis, A. B. McCoy, J. Chem. Phys. **122**, 044318 (2005).
[54] L. Wolniewicz, J. Chem. Phys. **103**, 1792 (1995); J. Komasa, K. Piszczatowski, G. Łach, M. Przybytek, B. Jeziorski and K. Pachucki, J. Chem. Theory Comput. **7**, 31053115 (2011).

[55] Supplementary Material

— Part A: *A summary of collision-time-delay approach to determination of energies and widths of quasi-bound states. SVD log-derivative method for evaluation of free-free and bound-free transtion amplitudes.*

— Part B: *Li^+-H_2 complex. Vibrational energy levels. Rotational energy levels. Infrared absorption spectrum.*

— Part C: *Li^+-D_2 complex. Vibrational and rotational energy levels. Details on application of the semi-rigid asymmetric top model. Properties of absorption spectrum (effects of ro-vibrational couplings, the role of d_X dipole component). Comparison with Li^+–H_2.*

— Part D: *Vibrational predissociation, perturbative analysis. Li^+-D_2 versus Li^+-H_2.*

— Part E: *Li^+-H_2 (D_2) versus He^+-H_2 (D_2). Isotope effects on vibrational predissociation.*